The Astrophysical Journal, 885:165 (17pp), 2019 November 10 https://doi.org/10.3847/1538-4357/ab4716

Investigating Early-type Galaxy Evolution with a Multiwavelength Approach. III. Insights from SPH Simulations with Chemophotometric Implementation

Paola Mazzei[1], Roberto Rampazzo[2], Antonietta Marino[1], Ginevra Trinchieri[3], Michela Uslenghi[4], and Anna Wolter[3]
[1] INAF Osservatorio Astronomico Padova, Vicolo dell'Osservatorio 5, I-35122, Padova, Italy; paola.mazzei@inaf.it
[2] INAF Osservatorio Astrofisico di Asiago, Via dell'Osservatorio 8, I-36012, Vicenza, Italy
[3] INAF Osservatorio Astronomico di Brera, Via Brera 28, I-20121, Milano, Italy
[4] INAF-IASF, Via E. Bassini 15, I-20133, Milano, Italy
Received 2019 March 22; revised 2019 September 13; accepted 2019 September 19; published 2019 November 12

Abstract

We are exploring galaxy evolution in low-density environments exploiting smooth particle hydrodynamic simulations, including chemophotometric implementation. From a large grid of simulations of galaxy encounters and mergers starting from triaxial halos of gas and dark matter, we single out the simulations matching the global properties of our targets. These simulations are used to give insights into their evolution. We focus on 11 early-type galaxies selected because of their nearly passive stage of evolution in the nuclear region. However, a variety of UV features are detected in more than half of these galaxies. We find no significant differences in the formation mechanisms between galaxies with or without UV features. Major and minor mergers are able to reproduce their peculiar UV morphologies, and galaxy encounters are more suitable for "normal" early-type galaxies. Their star formation rate self-quenches several gigayears later than the merger/encounter occurred via gas exhaustion and stellar feedback, moving the galaxy from blue to red colors and driving the galaxy transformation. The length of the quenching is mass-dependent and lasts from 1 to 5 Gyr or more in the less massive systems. All of our targets are gas-rich at redshift 1. Three of them assembled at most 40% of their current stellar mass at $z > 1$, and seven assembled more than 40% between redshift 0.5 and 1. Their stellar mass grows by 4% by crossing the green valley before reaching their current position on the NUV$-r$ versus M_r diagram.

Unified Astronomy Thesaurus concepts: Galaxy interactions (600); Galaxy masses (607); Computational methods (1965); Galaxy formation (595); Galaxy evolution (594); Galaxy quenching (2040); Galaxy ages (576); Galaxy dark matter halos (1880); Early-type galaxies (429)

1. Introduction

Our understanding of early-type galaxy (E+S0; hereafter ETG) evolution has been greatly improved in recent years thanks to multi-λ observations from satellites and ground-based telescopes. A relatively large amount of cold residual gas (10^7–10^9 $M_\odot$) is now considered a common property (50%) of these galaxies (e.g., Young et al. 2018, and references therein). The combination of the ultraviolet (UV) data provided by the *GALaxy evolution EXplorer* (*GALEX*; Martin et al. 2005) with the optical view given by the Sloan Digital Sky Survey (SDSS; Stoughton et al. 2002) has greatly undermined the standard picture of ETGs as passively evolving systems. Statistical studies (e.g., Kaviraj et al. 2007; Schawinski et al. 2007) found that about 30% of massive ETGs show recent/ongoing star formation (SF), with the largest incidence in galaxies located in low-density environments. However, ∼27/43% of cluster ETGs also show signatures of recent SF (Yi et al. 2011; Hernández-Pérez & Bruzual 2014, respectively). Found are UV-bright extended structures, e.g., rings, armlike features, and tails, sometimes completely distinct in shape from the optical galaxy body (Rampazzo et al. 2007, 2011, 2018; Jeong et al. 2009; Marino et al. 2009, 2011b, 2011a; Thilker et al. 2010) and often associated with H I emission (Salim & Rich 2010; Salim et al. 2012). The color–magnitude diagram (CMD) of the galaxies, using SDSS and *GALEX* magnitudes, (NUV–r) versus M_r, shows a strong morphological segregation: spirals lie in the blue cloud (BC), while ETGs are mainly located in the red sequence (RS; e.g., Yi et al. 2005; Salim et al. 2007; Wyder et al. 2007). An intermediate area called the green valley (GV) exists, irrespective of the environment. The CMD is a powerful diagnostic tool to detect very low levels of SF.

The spectral analysis with the mid-infrared (MIR) *Spitzer* IRS of a large number of ETGs within ≈2–3 $r_e/8$ highlighted the role of polycyclic aromatic hydrocarbon (PAH) features as tracers of episodes of SF that occurred between 1 and 2.5 Gyr ago, depending on metallicity (Bressan et al. 2006; Kaneda et al. 2008; Vega et al. 2010; Panuzzo et al. 2011; Nanni et al. 2013; Rampazzo et al. 2013). This paper, the third of a series based on *Swift* (Citterio et al. 1994; Gehrels et al. 2004; Burrows et al. 2005) multi-λ (XRT + UVOT) observations, is dedicated to tracing the evolution of 11 nearby ETGs (Table 1) living in low-density environments (Rampazzo et al. 2017, their Table 1) for which we collected a large, homogeneous, multi-λ data set, both from our previous papers (Trinchieri et al. 2015, hereafter Paper I; Rampazzo et al. 2017, hereafter Paper II) and from the literature, to constrain our simulations. Galaxies are selected because of the nearly passive stage of evolution of their nuclear region (Rampazzo et al. 2013). Most of these galaxies, which could be considered as templates of nearly dead ETGs, indeed show a manifold of bright and peculiar structures in *Swift*-UVOT images in the UV band (Figure 7 of Paper I). By analyzing their UV luminosity profiles, previously unexplored (Paper II), we found that this spectral range highlights the presence of a stellar disk. Moreover, accretion episodes have characterized the recent evolution of many of these ETGs. Such episodes left signatures of recent SF in the nuclei and/or in the galaxy outskirts. The recent SF points toward wet accretion episodes, since

Table 1
The Sample of ETGs

Galaxy	D_{25} (arcmin)	D (Mpc)	Scale (kpc arcmin^{-1})	m–M (mag)	M_B (mag)	$M_{\rm H\,I}$ ($10^9\,M_\odot$)	L_X(gas) (10^{40} erg s^{-1})
(1)	(2)	(3)	(4)	(5)	(6)	(7)	(8)
NGC 1366	2.1	21.1 ± 2.1	6.1	31.62 ± 0.50	-18.89 ± 0.54	<1.0	<0.03
NGC 1415	3.7	22.7 ± 2.5	6.5	31.78 ± 0.55	-19.23 ± 0.55	1.2[a]	0.1
NGC 1426	2.9	24.1 ± 2.4	7.0	31.91 ± 0.50	-19.71 ± 0.52	....	<0.03
NGC 1533	3.2	21.4 ± 2.1	6.2	31.65 ± 0.50	-19.93 ± 0.52	7.4[b]	<0.11
NGC 1543	3.6	20.0 ± 2.0	5.8	31.50 ± 0.50	-20.13 ± 0.53	0.8	<0.16
NGC 2685	4.4	16.0 ± 1.6	4.8	31.02 ± 0.50	-19.13 ± 0.51	3.0[c]	<0.04
NGC 2974	3.5	21.5 ± 2.0	6.2	31.66 ± 0.46	-20.01 ± 0.60	0.7[d]	0.2
NGC 3818	2.4	36.3 ± 3.6	10.4	32.80 ± 0.50	-20.26 ± 0.58	...	0.55
NGC 3962	4.2	35.3 ± 3.5	10.2	32.74 ± 0.50	-21.32 ± 0.53	2.8[e]	0.33
NGC 7192	2.4	37.8 ± 3.8	10.7	32.89 ± 0.50	-20.84 ± 0.51	0.7[e]	1.0
IC 2006	2.3	20.2 ± 2.0	5.9	31.53 ± 0.50	-19.34 ± 0.51	0.3	0.08

Notes. The apparent diameters (column 2) and adopted distances (column 3) are derived from the Extragalactic Distance Database (EDD; http://edd.ifa.hawaii.edu), as in Papers I and II. The absolute total magnitudes in column 6 are derived from column 5 using B-band observed total magnitudes and extinction corrections from the HyperLeda catalog (http://leda.univ-lyon1.fr; Makarov et al. 2014). The H I masses (column 7) are obtained using distances in column 3 and 1.4 GHz fluxes from the NASA/IPAC Extragalactic Database (NED), operated by the Jet Propulsion Laboratory, California Institute of Technology, under contract with the National Aeronautics and Space Administration.

[a] Courtois & Tully (2015).
[b] Ryan-Weber et al. (2003).
[c] Józsa et al. (2009).
[d] Kim et al. (1988).
[e] Serra & Oosterloo (2010). The X-ray gas luminosities (column 8) are from Table 7 of Paper I.

dissipation is the source of the underlying disk structure highlighted by the analysis (Paper II).

Morphology, colors, and star formation rate (SFR) primarily depend on the small-scale (<1 Mpc) environment (Hogg et al. 2004; Kauffmann et al. 2004; Wetzel et al. 2012). This result has been extended by studying galaxy group samples; they show that colors and SF history most directly depend on the properties of the host dark matter (DM) halo (Blanton & Berlind 2007; Wei et al. 2010; Tinker et al. 2012), in agreement with the results of smooth particle hydrodynamic (SPH) simulations by Mazzei & Curir (2003, hereafter MC03). In this context, the investigation of the evolution of group members in the nearby universe acquires a great cosmological interest because more than half of galaxies reside in such environments. Furthermore, since the velocity dispersion of galaxies is significantly lower in groups than in clusters, the merger probability and the effects of interaction on galaxy evolution are much higher. Consequently, groups provide a zoom-in on phenomena driving the galaxy evolution before the galaxies fall into denser environments (e.g., Wilman et al. 2009; Just et al. 2010). Starting from the pioneering works of Toomre & Toomre (1972, and references therein), several papers contributed to shed light on the important role of mergers/interactions in galaxy evolution—Toomre (1977), Combes et al. (1990), Mihos & Hernquist (1994, 1996), Barnes & Hernquist (1996), Naab & Burkert (2003), Bournaud et al. (2005), and Di Matteo et al. (2007), to name a few—up to the most recent papers of Eliche-Moral et al. (2018) and Martin et al. (2018, and references therein). The dissipative merger simulations of Eliche-Moral et al. (2018) start from systems just formed, composed of a spherical nonrotating DM halo, and by a disk of gas particles with or without the presence of a stellar bulge. These simulations explore about 3–3.5 Gyr of evolution. Martin et al. (2018) focused on processes triggering galaxy transformations of massive galaxies ($M > 10^{10}\,M_\odot$) exploiting cosmological hydrodynamic simulations by Kaviraj et al. (2017). These simulations, based on an adaptive mesh refinement code (RAMSES) and including the baryon treatment with stellar and active galactic nucleus (AGN) feedback, are able to resolve baryonic physics on kiloparsec scales, larger than we use in this paper (Section 3). They derived important statistical assessments about the processes that drive morphological transformation across cosmic time.

We explore the merger/interaction scenario focusing on low-density environments. Our simulations start from collapsing triaxial systems composed of DM and gas and combine the SPH code with chemophotometric implementation based on evolutionary population synthesis (EPS) models (SPH-CPI simulations) providing the spectral energy distribution (SED) at each snapshot. From a large grid of SPH-CPI simulations, we select for each galaxy the one that matches the current global properties of our target, in particular, (i) the SED extended over 4 orders of magnitude in λ, (ii) the absolute B-band magnitude, and (iii) the optical and UV morphologies, as confirmed by (iv) the luminosity profiles. Moreover, the selected simulation must account for (v) the H I gas mass, (vi) the hot gas X-ray luminosity, and (vii) the available kinematic data. These simulations, anchored to the local properties of our targets, are used to give insights into galaxy evolution and, in particular, to shed light on their quenching phase, which is identified by their rest-frame CMDs. Therefore, we study the galaxy transformation by looking at the behavior of SFR, gas accretion history, total mass growth of different components (baryons, stars, DM), and, in particular, the CMD. This is a useful tool to capture a very low level of residual SF, highlighting the length of different phases leading to quenching and galaxy transformation from the BC to the RS.

The SED accounts for chemical evolution, stellar emission, internal extinction, and re-emission by dust in a self-consistent way, as described in previous works (Spavone et al. 2009, 2012, and references therein). This extends more than 4 orders of magnitude in wavelength, from 0.05 to 1000 μm. Each simulation in the grid self-consistently provides

morphological, dynamic, and chemophotometric evolution. We already applied the same approach to ETGs belonging to the groups USGC 367 and LGG 225 (Mazzei et al. 2014a) and to two S0 galaxies, namely, NGC 3626 and NGC 1533, in Mazzei et al. (2014b), where we match photometric, structural (e.g., disk versus bulge), and kinematical (gas versus stars) properties, showing that a major merger (1:1) accounts for the structural and photometric transformations expected in these systems (Querejeta et al. 2015). Furthermore, our approach allowed us to fit the current global properties of (i) several other ETGs (Spavone et al. 2009, 2012; Bettoni et al. 2011, 2012, 2014; Trinchieri et al. 2012), (ii) the blue dwarf galaxy UGC 7639 (Buson et al. 2015), (iii) a few late-type galaxies (LTGs) of different luminosity classes (Bettoni et al. 2011, 2014; Mazzei et al. 2018), (iv) the pre-merger case NGC 454 (Plana et al. 2017), and (v) the false pair NGC 3447/3447A (Mazzei et al. 2018), showing that this a powerful tool to investigate galaxy evolution.

The plan of the paper is the following. In Section 2 we review the galaxy sample, and in Section 3 we summarize the recipes of our SPH-CPI simulations. We obtain the evolution of these galaxies anchoring the simulations to match the global current properties of each ETG. The results are presented in Section 4, while the details of the fit of each target are listed in the Appendices A and B. Discussion and conclusions follow in Sections 5 and 6 respectively.

Hereafter, we use the following cosmological parameters: $H_0 = 67$ km s^{-1} Mpc^{-1}, $\Omega_\Lambda = 0.68$, $\Omega_{\rm matter} = 0.32$ (Planck Collaboration XVI 2014; Calabrese et al. 2017), which correspond to a Λ cold dark matter (ΛCDM) model with a universe age of 13.81 Gyr (Calabrese et al. 2017, their Table 1) and light-travel time (look-back time) of 7.98 Gyr at $z = 1$ and 5.23 Gyr at $z = 0.5$.

2. The Sample

The sample is presented in Table 1, where all of the main observed characteristics are listed for each galaxy. All galaxies are classified as ETGs (see Paper II, Table 1). A transition case between early and later types is NGC 1415, whose classification, however, has a large uncertainty (Paper II). Their absolute M_B magnitudes, from -18.9 to -21.3 mag, are all extinction-corrected. These ETGs are gas-rich, on average, with H I masses of the order of $10^9\,M_\odot$. Table 1 of Paper II collects their environmental properties, which span a large range of local densities: $0.13 \leqslant \rho_{xyz}\,({\rm gal\ Mpc^{-3}}) \leqslant 0.95$. We select here only galaxies with the nuclear region 2–3 $\times\ r_e/8$ in a nearly passive stage of evolution (column 4 in Table 1 of Paper I). Many of these galaxies, which could be considered as templates of nearly dead ETGs, nonetheless show a manifold of bright and peculiar structures in *SWIFT*-UVOT images in the UV band. Their UV and optical images have been presented for each band in Figure 7 of Paper I. Their three-color composite images, both in the UV and in the optical bands, are shown in Figures 4–14 of Paper II. We showed in that paper that a single Sérsic law (Sérsic 1968) is a good fit to their surface brightness luminosity profiles with decreasing values of the Sérsic index, n, for decreasing wavelength. The Sérsic law is widely used for ETGs, since it is a generalization of the $r^{1/4}$ de Vaucouleurs (1948) law (see, e.g., Caon et al. 1993). Special cases are $n = 1$, the value for an exponential profile, and $n = 0.5$ for a Gaussian luminosity profile. Galaxies with n higher than 1 have a steep luminosity profile in their nuclear regions and extended outskirts. Values lower than 1 indicate a flat nuclear region and more sharply truncated outskirts (see also Paper II). The values of their UV Sérsic indices highlighted the presence of underlying disks and the role of dissipative mechanisms.

According to their UV morphology from Paper II, the sample can be divided into two sets. Five ETGs, namely, NGC 1366, NGC 1426, NGC 3818, NGC 3962, and NGC 7192, do not show any remarkable features in both the optical and UV bands. The remaining six ETGs, namely, NGC 1415, NGC 1533, NGC 1543, NGC 2685, NGC 2974, and NGC IC 2006, show bright, peculiar, ring/armlike UV features.

3. SPH-CPI Simulations

We have performed a large grid of SPH-CPI simulations of galaxy encounters and mergers starting from triaxial systems initially composed of DM and gas. As described in several previous works (Mazzei et al. 2014a, 2014b, 2018), for each galaxy, we single out the simulation that matches the current global properties of our target (see Table 1), in particular, (i) the SED extended over 4 orders of magnitude in λ, (ii) the absolute B-band magnitude, and (iii) the optical and UV morphologies, as confirmed by (iv) the luminosity profiles. Moreover, the selected simulation must account for (v) the H I (cold) gas mass, (vi) the hot gas X-ray luminosity, and (vii) the available kinematic data from the HyperLeda catalog. The simulation that contains the snapshot that best reproduces all of these observational constraints also provides insights on the galaxy evolution.

All of the simulations start from collapsing triaxial systems composed of DM and gas in different proportions and total masses, as in Curir & Mazzei (1999) and Mazzei & Curir (2003). In particular, all of the simulated halos have the same initial conditions, that is, virial ratio (0.1); average density, to avoid different collapse times; and a spin parameter equal to 0.06 aligned with the shorter principal axis of the DM halo. The initial triaxiality ratio of the DM halos as detached by the Hubble flow in a CDM scenario, $\tau = (a^2 - b^2)/(a^2 - c^2)$, is 0.84 (Mazzei et al. 2014a, 2014b), where $a > b > c$. This τ value is different from the fiducial value adopted by MC03 (0.58) and motivated to be closer to the initial condition of cosmological halos as in Warren et al. (1992), Curir et al. (2006, their Table 1), and Schneider et al. (2012). The simulations include self-gravity of gas, stars, and DM; radiative cooling; hydrodynamical pressure; shock heating; viscosity; SF; feedback from evolving stars and Type II supernovae (SNe); and chemical enrichment. The initial mass function (IMF) is of the Salpeter type (Salpeter 1955) with upper and lower mass limits of 100 and $0.01\,M_\odot$. All of the model parameters had been tuned in previous papers devoted to analyzing the evolution of isolated collapsing triaxial halos initially composed of DM and gas (Curir & Mazzei 1999; Mazzei 2003; MC03). In those papers, the role of the initial spin of the halos, their total mass and gas fraction, and triaxiality ratio, as well as different IMFs, particle resolutions, SF efficiencies, and values of the feedback parameter, were all examined. In particular, a slightly higher SFR compared with the other possibilities examined arises from our choice of IMF parameters (see MC03, their Figure 1); this allows for the lowest stellar feedback strength (63% less than that in the same simulation with a lower mass limit of $0.1\,M_\odot$ instead of $0.01\,M_\odot$) and the expected rotational support when disk galaxies are formed (MC03). As pointed out by Kroupa

Table 2
Initial Parameters of SPH-CPI Simulations Reproducing the 11 ETGs

Name	$M_{\rm tot}$ ($10^{10}\,M_\odot$)	Mass Ratio	$f_{\rm gas}$	$N_{\rm part}$	r_1 (kpc)	r_2 (kpc)	v_1 (km s^{-1})	v_2 (km s^{-1})	Spins	m/e
NGC 1366	110	10:1	0.1	2.2×10^5	85	847	7	70	↕	e
NGC 1415	600	5:1	0.02	1.2×10^5	206	1032	26	82	∥	m
NGC 1426	200	1:1	0.1	8.0×10^4	327	327	71	71	∥	m
NGC 1533	300	2:1	0.1	6.0×10^4	155	311	60	119	⊥	m
NGC 1543	240	5:1	0.1	9.6×10^4	78	389	27	134	∥	m
NGC 2685	150	2:1	0.1	6.0×10^4	311	621	29	60	⊥	m
NGC 2974	400	1:1	0.1	8.0×10^4	466	466	73	73	∥	m
NGC 3818	400	1:1	0.1	6.0×10^4	233	233	104	104	∥	m
NGC 3962	550	10:1	0.1	1.1×10^5	177	1779	10	104	∥	e
NGC 7192	400	1:1	0.1	6.0×10^4	466	466	73	73	∥	m
IC 2006	300	2:1	0.1	6.0×10^4	155	311	60	119	↕	m

Note. Our targets are in column 1, the total mass of the simulation selected is in column 2, the halo mass ratio is in column 3, the initial gas fraction is in column 4, the initial number of particles is in column 5, the positions and velocities of the two halos with respect to the mass center of the system are in columns 6–9, and the halo spin direction (∥ parallel, ⊥ perpendicular, ↕ counterrotating) are in column 10; the label in column 11 indicates whether the simulation gives rise to a merger (m) or an encounter/flyby (e).

(2012), this slope is almost the same as the universal mass function that links the IMF of galaxies and stars to those of brown dwarfs, planets, and small bodies (meteoroids, asteroids). The integrated properties of simulated galaxies stopped at 15 Gyr have been successfully compared with those of local galaxies (Curir & Mazzei 1999, e.g., their Figure 17; Mazzei 2003, 2004, their Figure 8). This means that their colors, absolute magnitudes, metallicities, and mass-to-luminosity ratios all match the results of simulations. Each simulation self-consistently provides morphological, dynamic, and chemophotometric evolution, namely, the SED, at each evolutionary time (which we call a "snapshot"). The SED accounts for chemical evolution, internal extinction, and re-emission by dust in a self-consistent way. This extends more than 4 orders of magnitude in wavelength, from 0.05 to 1000 μm. Additionally, we derive the X-ray luminosity of the hot gas ($T \geqslant 3 \times 10^6$ K) in the 0.5–2 keV spectral range, following prescriptions discussed in Paper I.

Each simulation of our grid of galaxy mergers and encounters starts from systems built up with the initial conditions listed in Table 1 and the parameters tuned as in the above cited papers, as described in Mazzei et al. (2014a, 2014b, 2018). This set accounts for different masses (from 10^{13} to $10^{10}\,M_\odot$ for each system), mass ratios (from 1:1 to 10:1), gas fractions (from 0.1 to 0.01), and particle resolutions (initial number of gas and DM particles from 60,000 to 220,000). By seeking to exploit a wide range of orbital parameters, we varied the orbital initial conditions in order to have the first pericenter separation, p, equal to the initial length of the major axis of the more massive triaxial halo down to 1/10 of the same axis for the ideal Keplerian orbit of two points of given masses. For each value of p, we changed the eccentricity in order to have hyperbolic orbits of different energy. The spins of the systems are generally parallel to each other and perpendicular to the orbital (XY) plane. Misaligned spins have also been analyzed in order to investigate the effects of the system initial rotation on the results. Table 2 reports the initial conditions of each simulation that best reproduces, at a given snapshot, the global current properties of our targets. We recall here that by major mergers, we mean mergers with the initial mass ratio of halo progenitors (Table 2) $\leqslant$4, while in minor mergers, the ratio is >4. In particular, column 5 provides the total initial number of particles (the number of gas particles is the same as DM ones). The initial gas mass resolution, $m_{\rm gas}$, is between 1×10^6 and $1.33 \times 10^7\,M_\odot$. The SF efficiency is 0.4, and the stellar mass resolution in each simulation ranges from $0.4 \times m_{\rm gas}$ to $0.04 \times m_{\rm gas}$ (e.g., Mazzei et al. 2014a), that is, for simulations in Table 2, (0.40–52) $\times 10^5\,M_\odot$. As a comparison, the mass resolution range of Eliche-Moral et al. (2018) is (3.5–20) $\times 10^5\,M_\odot$. Recent cosmological simulations of Kaviraj et al. (2017) and Martin et al. (2018) have mass resolution of $\simeq 2 \times 10^6\,M_\odot$. The time step between individual snapshots is 37 Myr. The gravitational softening is 1, 0.5, and 0.05 kpc for DM, gas, and star particles, respectively. Our stellar spatial resolution, limited by softening length, is 50 pc, to be compared with 200 pc as the best spatial resolution of Eliche-Moral et al. (2018) and $\approx$1 kpc in Martin et al. (2018). The final number of particles is at least twice that of the initial number, ranging from about 1.33 to 3.65×10^5. We point out that the resulting SFR, the driver of the evolution, converges when the initial particle number is above 10^4 (MC03, their Figure 1; Christensen et al. 2010, 2012). The main results are presented in the next section. The details of the match of each target from the simulation that best reproduces its morphological, photometric, and kinematical properties are reported in the Appendix.

4. Results

From our grid of SPH-CPI simulations, we concentrate on the one simulation that provides a snapshot that convincingly reproduces the global properties of the ETGs considered, accounting for the following observational constraints: (i) total absolute B-band magnitude within the range allowed by observations (Table 1), (ii) integrated SED as the observed one (see Figure 1), (iii) UV and optical morphologies (see Figure 2) confirmed by a (iv) comparison between luminosity profiles (see Figure 3), (v) kinematical properties in agreement with those in the literature, (vi) X-ray luminosity of the hot gas, and (vii) the amount of cold gas consistent with the data in Table 1 (see the Appendix). The results we present in Figures 4 and 5, as we clarify below, are evolutionary behaviors from the

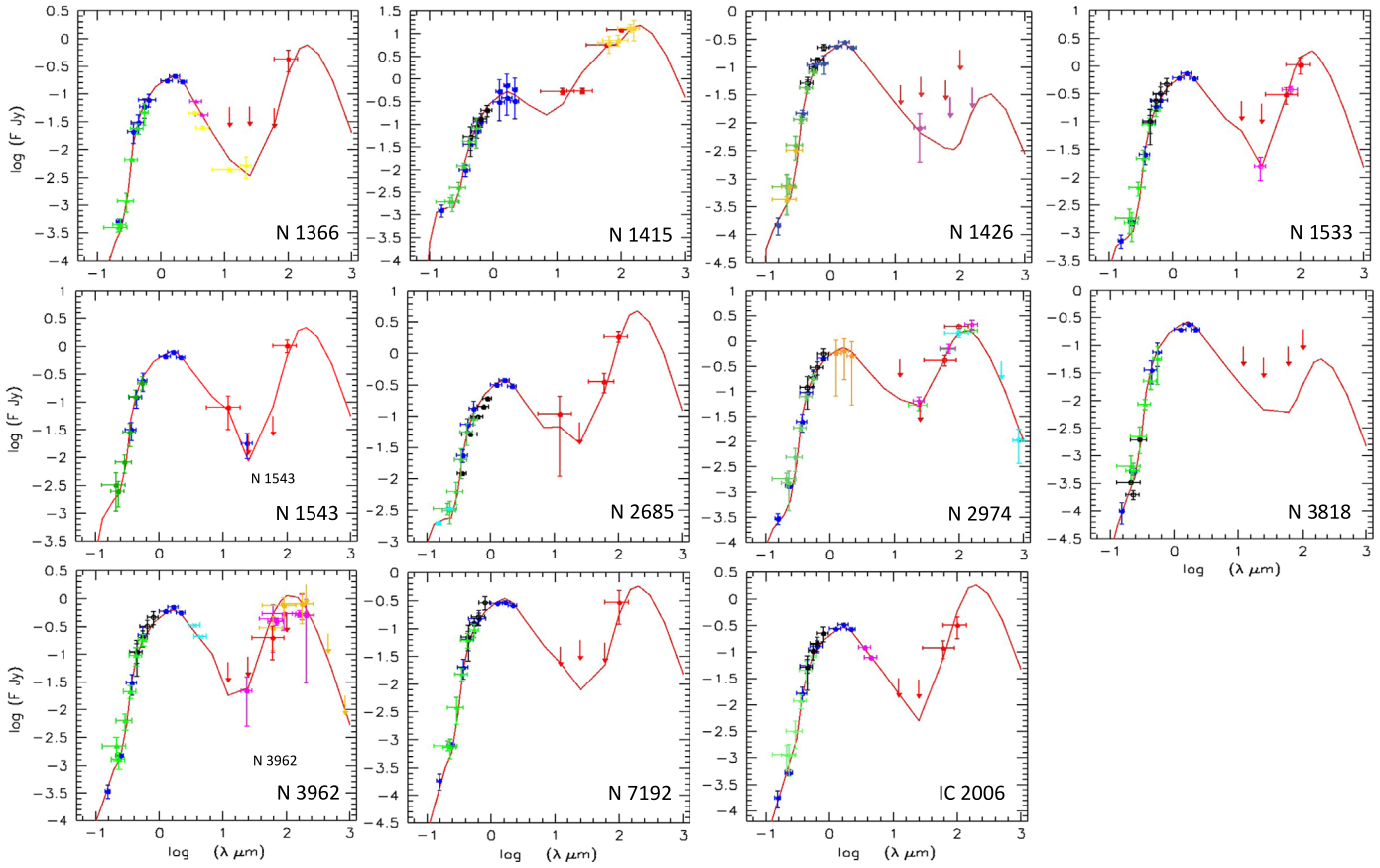

Figure 1. The SEDs of our targets (colored points) compared with predictions from the SPH-CPI simulations in Table 2 (red solid lines) at the galaxy ages in Table 3. Green triangles are Swift-UVOT magnitudes from Paper II, blue filled circles are from NED, black circles are from the CGS catalog (Ho et al. 2011; Li et al. 2011), and red points are IRAS fluxes from NED; other details are in the Appendix. Data are corrected for our own galaxy extinction following the prescription of NED and Paper II in the Swift-UVOT filters.

simulation that best accounts for all of the points above (i–vii) at the same snapshot. This snapshot sets the age of the galaxy accounted for from the onset of the SF. The galaxies studied span a large range of ages, between 9.6 Gyr for NGC 3962 and 13.8 Gyr for IC 2066, the oldest galaxy in our sample (Table 3), and total stellar masses, from 3.7 to 24.4 $\times$ $10^{10}\,M_{\odot}$ (Table 3), with the most massive, NGC 3962, also being the youngest. The absolute magnitudes derived from the snapshots best fitting the global properties of our targets are reported in Table 3 and are to be compared with the observed ones in Table 1. Figure 1 allows the comparison between the observed SEDs, extended over almost 4 orders of magnitude in wavelength, and those derived from the selected snapshot (red solid line). Error bars account for bandwidth (x-axis) and 3σ uncertainties of the flux (y-axis). The snapshot far-IR (FIR) SED is always composed of warm and cold dust components, both including PAH molecules as described in Mazzei et al. (1992, 1994), and Mazzei & De Zotti (1994). The warm dust component is heated by massive stars in H II regions and the cold one by the diffuse light in the galaxy. The UV and optical morphologies are compared in Figure 2 with simulations in the same field of view and with the same resolution of the data. In order to derive the general trend of the underlying structure, the corresponding luminosity profiles are compared in Figure 3. Properties at points (v)–(vii) above are discussed for each target in the dedicated section in the Appendix. Table 3 summarizes the global properties of the simulations in Table 2 from the snapshot best describing the current properties of our targets.

The relevant evolutionary properties are shown in Figures 4 and 5. These include five panels for each target highlighting connections between general evolution and the path in the CMD. This path shows the behavior of the SFR, including how each galaxy transforms and quenches. The NUV$-r$ color is an excellent tracer of even small amounts of SF (e.g., Mazzei et al. 2014a). The first three panels of Figures 4 and 5, from top to bottom, show the gas accretion history, SFR, and mass assembly history derived within a fixed reference radius of 50 kpc, centered on the B-band luminous center of the galaxy. The black solid line in the top panels corresponds to the total mass of gas, the blue dashed line corresponds to gas with a temperature $\leqslant 10^4$ K, and the red dotted line corresponds to gas with a temperature $\geqslant 10^6$ K. Here, as in the following, we refer to cold gas as that with a temperature $\leqslant 10^4$ K, given that its cooling timescale is shorter than the snapshot time resolution (0.037 Gyr). This represents the upper limit of H I provided by each simulation. The SFR is shown with a blue solid line that becomes red as merger begins (when there is a merger), namely, when the two stellar systems can no longer be distinguished because their mass centers cannot be identified/separated anymore. We find that the SFR shows a gentle self-quenching after reaching its maximum value, due to gas exhaustion and stellar feedback, lasting several Gyr in all of our targets, with the exception of NGC 3818. This galaxy reaches the highest value of the SFR among the targets examined ($168\,M_{\odot}$ yr^{-1}; see the Appendix). The mass assembly history, that is, the evolution of different mass components, is shown

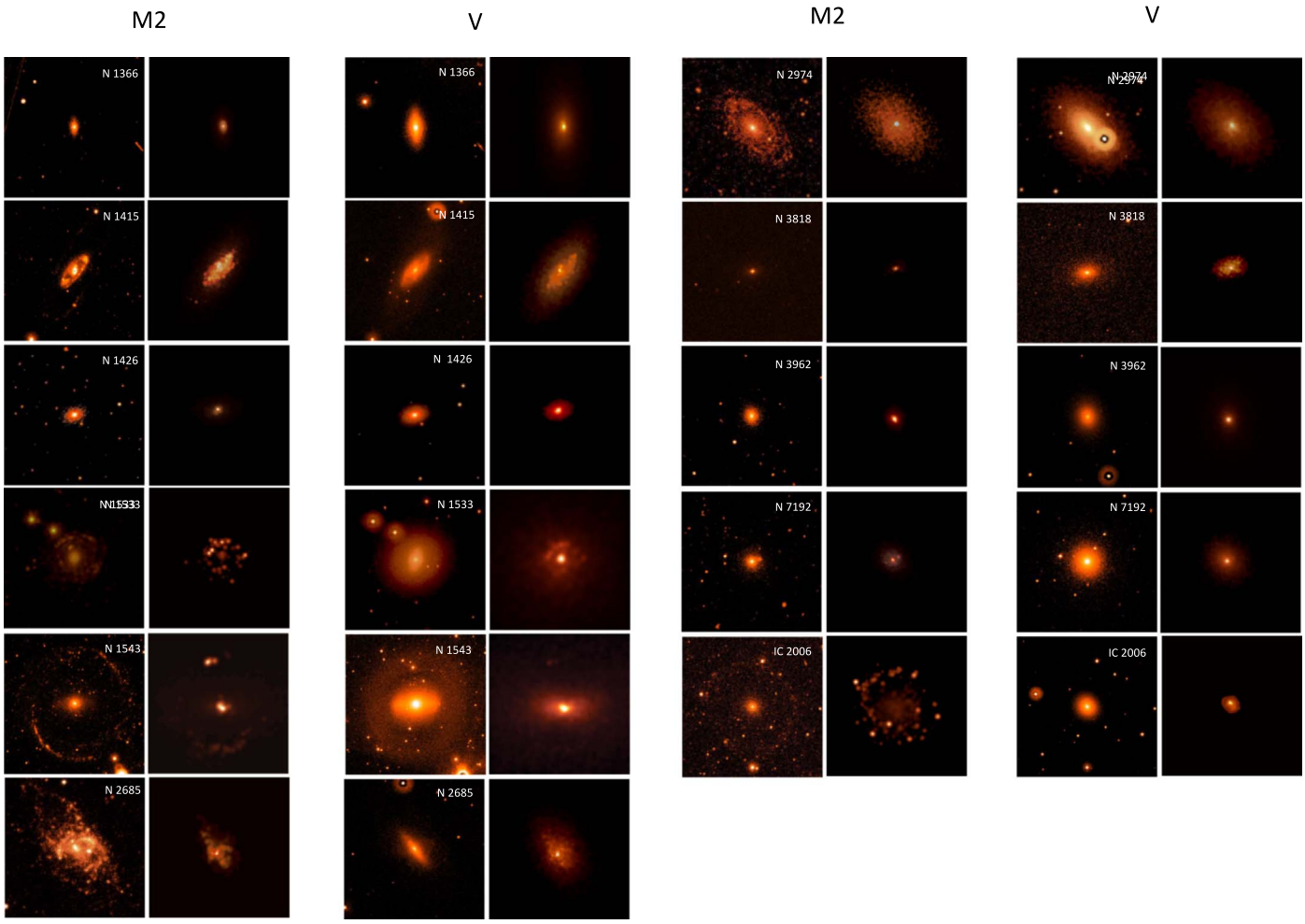

Figure 2. Observed vs. simulated image of the 11 galaxies. In each panel, the left column shows the Swift-UVOT M2- (first and fifth columns) or *V*- (third and seventh columns) band image; the right column shows the simulated image with the same field of view and resolution ($1''$ pixel^{-1}) of the observed one. All images are $5' \times 5'$, except for NGC 1415 with $8\farcm6 \times 8\farcm6$ and IC 2006 and NGC 2685 with $7' \times 7'$.

within two fixed reference radii, 50 kpc and R_{25}, in panels three and four of Figures 4 and 5 (see also Table 1) to highlight their different behavior. The black solid line is the total mass, the red short-dashed line is the DM, the blue dotted line is the gas +stars (baryons), and the magenta long-dashed line is the stellar component. The evolution is stopped at 14 Gyr (cf. Section 1) in all panels. We find that the DM mass always exceeds the stellar mass within the larger radius, and their mass ratio sets on a constant value while the SF quenches. An opposite behavior occurs within the smaller radius, where the stellar mass exceeds the DM while the SF quenches. The bottom panels present the path of the galaxy in its rest-frame optical–UV CMD. In the following, as in Mazzei et al. (2014a), we assume that the GV lies between NUV–$r = 3.5$, which marks the GV entry, and NUV–$r = 5$, the RS threshold. Significant evolutionary stages are outlined by black dots, and red triangles correspond to $z = 1$ and 0.5 using the cosmological parameters in Section 1. The red and blue local ($z = 0$) sequences are reported following the prescriptions in Wyder et al. (2007). Each galaxy moves along the BC until reaching its maximum SF, which corresponds to the brightest point (BP) of its CMD. Then, the SFR fades, and the quenching begins. This causes the crossing of the BC and GV. The five galaxies of our sample without UV features all belong to the RS. Of the six showing UV features, two—NGC 1415 and NGC 2685—belong to the GV. The evolution of NGC 1543, which belongs to the RS, shows short rejuvenation episodes in the last 2.3 Gyr. Rapid oscillations also appear along the path of NGC 1415 (see the SFR panels). Both NGC 1543 and NGC 1415 are minor mergers (Table 2). The interaction/merger, which occurred in the galaxy's past, produces the potential well and gas reservoir that drive the gas assembly history. The growth of the stellar mass develops from the SFR driven by this accretion history. The quenching, which gives rise to galaxy transformation, occurs from the behavior of the SFR, that is, gas exhaustion and stellar feedback, several gigayears after the start of the interaction/merger. Therefore, the merger or interaction is not the actual main cause of the SF quenching. Rather, this is a consequence of the galaxy evolution, and it is related to gas exhaustion and stellar feedback. The SN feedback is enough to allow quenching of our targets whose total stellar masses range from 3.7 to 24.4 $\times 10^{10} M_{\odot}$, while the total masses range from 16.8 to 61.2 $\times 10^{10} M_{\odot}$ (Table 3).

5. Discussion

We find that there are no significant differences in the formation mechanisms between ETGs with or without UV features. Among those with UV features, NGC 1543 and NGC 1415 are minor mergers, and NGC 1533, NGC 2685,

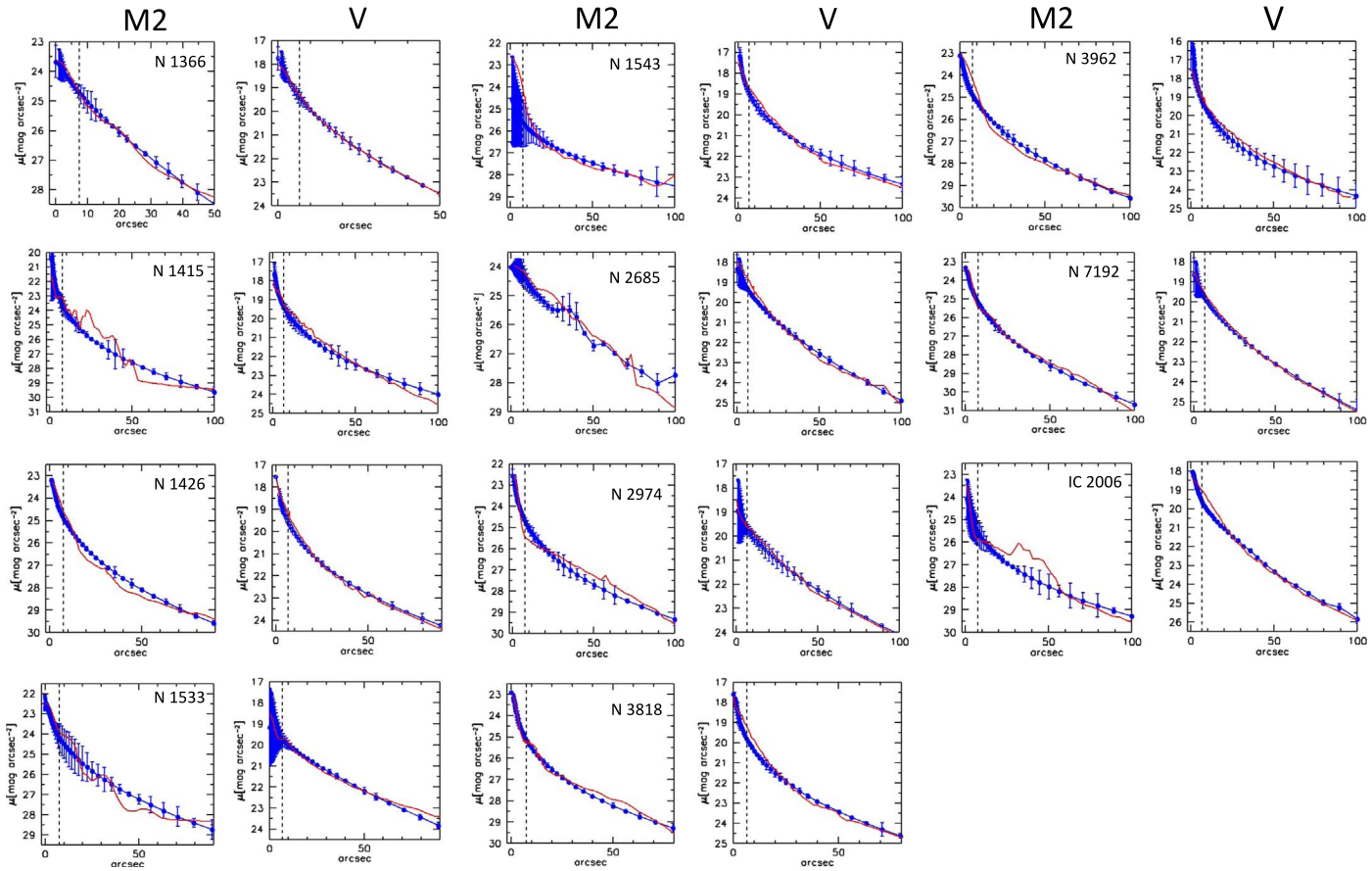

Figure 3. Luminosity profiles of our targets in the Swift-UVOT M2 and *V* bands. Blue dots are Sérsic functions in Paper II, and red solid lines are from the simulation snapshots in Figure 2.

NGC 2974, and IC 2006 are major mergers. Among the normal (no UV features) ETGs, NGC 1366 and NGC 3962 are due to encounters, or flyby, with a very small companion (mass ratio 10:1), and NGC 1426, NGC 3818, and NGC 7192 are major mergers. Therefore, major mergers reproduce well the current global properties of ETGs both with long-lasting (several gigayears) and without UV features, minor mergers look more suited to ETGs with short times ($\leqslant$0.5 Gyr) but long-lived UV features, and galaxy encounters with a small companion well match normal ETGs. Minor mergers analyzed here produce rejuvenation episodes that move the galaxies from the RS back to the GV (Figure 5, bottom panels). Moreover, while these galaxies cross the GV or return to the GV region, they are characterized by extended features in their UV morphologies.

Table 4 and Figure 6 summarize the growth of the stellar mass within two fixed reference radii (Section 4) of simulations in Table 2. We find that all galaxies in our sample assembled at least 60% of their stellar mass within 50 kpc at $z \leqslant 1$. At $z > 1$, 45% of our sample, namely, NGC 1366, NGC 1451, NGC 1543, NGC 2685, and NGC 3962, accreted less than 20% of their actual mass; NGC 3818 and IC 2006 accreted about 20%; and NGC 1426, NGC 1533, and NGC 2974 accreted about 40%.

The maximum SFR occurred more than 3 Gyr ago in about 73% of our targets and between 2 and 3 Gyr ago in the remaining three cases, namely, NGC 2685 at $z = 0.15$ (2 Gyr), NGC 3962 at $z = 0.17$ (2.2 Gyr), and NGC 7192 at $z = 0.20$ (2.5 Gyr). In four galaxies, this maximum occurred at $z > 0.5$, that is, more than 5.2 Gyr ago. These are NGC 1426 among UV featureless ETGs and NGC 1415, NGC 1533, and NGC 2974 among those with UV features.

At most 4% of their total stellar mass was assembled after leaving the BC (GV–0 in Table 4). As we noted above, NGC 2685 corresponds to a late merger, occurring 6 Gyr ago, at $z = 0.61$. All other mergers took place at redshift $\geqslant$1; therefore, the age of the merger is $\geqslant$8 Gyr (Figure 7). In this figure, as in the following one (Figure 8), we also include eight ETGs in two nearby groups, USGC U367 and LGG 225, studied in Mazzei et al. (2014a). We extracted simulations from the same grid for these further galaxies to match their global properties. Therefore, we increase the sample to 19 objects. The span in stellar masses for the additional sample is (0.32–19.81) $\times 10^{10} M_{\odot}$, and that in total masses is (2.78–63.47) $\times 10^{10} M_{\odot}$. Thus, the total range of stellar masses explored, (0.32–24.4) $\times 10^{10} M_{\odot}$, is about 2 orders of magnitude. Figure 8 shows that the time spent crossing the GV reduces with increasing luminosity of the BP of the CMD (left) and current stellar mass (right). The correlation indexes are 0.72 and −0.67, respectively. This indicates that more massive galaxies supported higher SFRs in the past (Mazzei & Curir 2003; Rodighiero et al. 2011, and references therein) and crossed the GV more quickly. Massive galaxies have undergone a faster morphological transformation from blue to red colors (e.g., Mazzei et al. 2014b) than less massive ones. Therefore, the evolution toward ETG appears to be mass-dependent. The transit time of the GV traces this transition, lasting some gigayears. During this phase, the SF is quenching, and the relaxed shape of

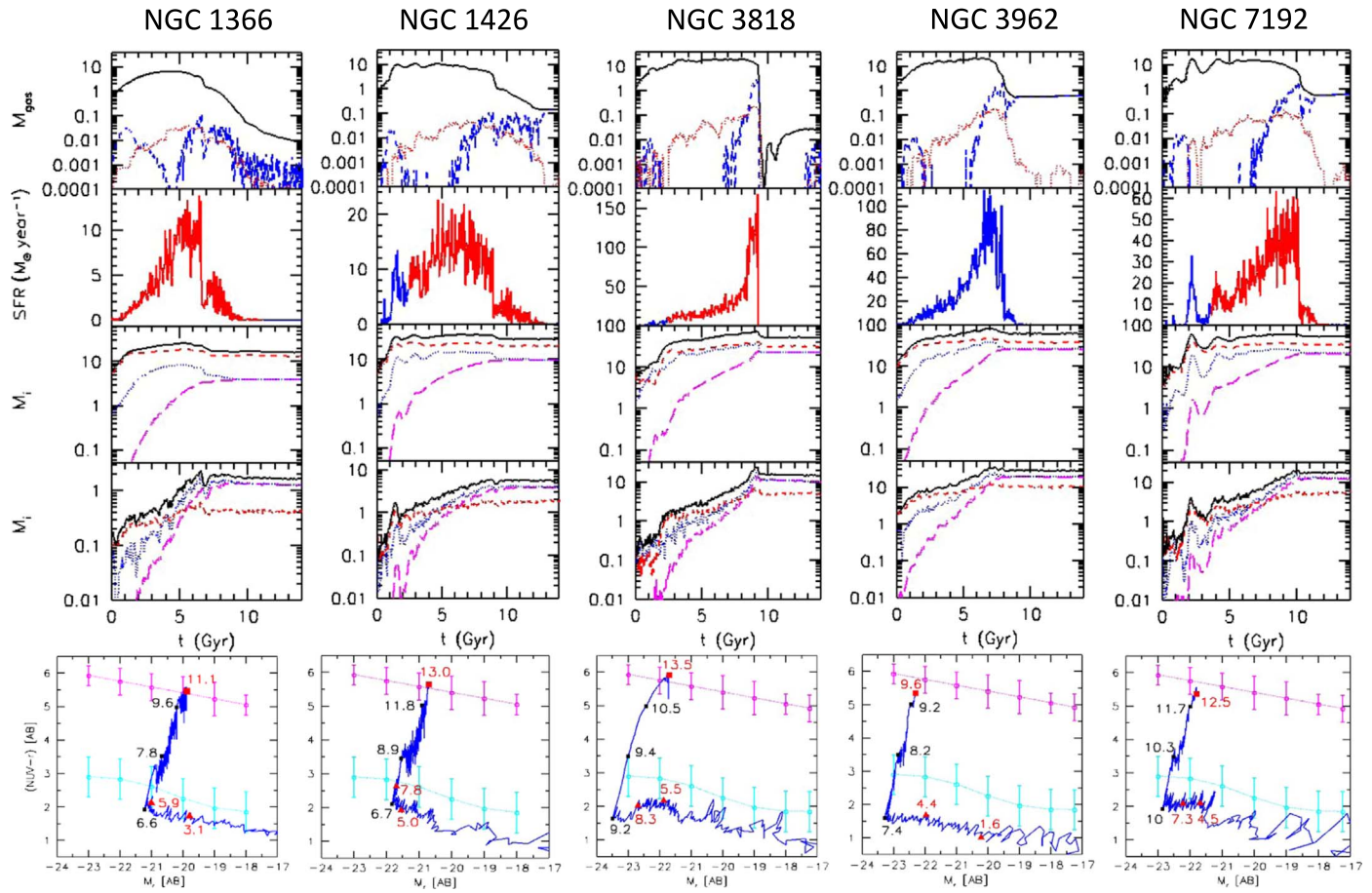

Figure 4. Evolutionary properties of ETGs without UV features. From top to bottom: gas accretion history; SFR (red line from the beginning of the merger as defined in Section 4); mass assembly history (see also Table 4) within 50 kpc and R_{25} in Table 1, both centered on the B-band luminous center of the galaxy; and CMD in the galaxy rest frame. More details are given in Section 4. The $M_{\rm gas}$ and the different mass components, M_i, are in units of $10^{10}\,M_{\odot}$.

these systems as we see them today is being produced (Mazzei et al. 2014b). Dissipative merger simulations by Eliche-Moral et al. (2018), which start from systems composed by a spherical nonrotating DM halo and a disk of gas and star particles with or without the presence of a stellar bulge, also predict that the length of the relaxation process is of some gigayears. The interaction/merger occurred in the galaxy's past at a redshift higher than 1, on average (Figure 6, right panel), and drives the gas assembly history that regulates the SFR and, as a consequence, the galaxy evolution and transformation. Moreover, the merger and interaction are not the main reasons for the SF quenching. Rather, this is a consequence of the galaxy evolution, and it is related to gas exhaustion and stellar feedback. This picture is consistent with recent findings by Eales et al. (2017, 2018a, 2018b), Bremer et al. (2018), and Kelvin et al. (2018). Eales et al. (2017) analyzed a volume-limited sample of 323 nearby galaxies from the Herschel Reference Catalogue (Boselli et al. 2010) and investigated their SFR versus mass properties using several indicators. The sample is considered representative of the end point of the galaxy evolution in the last 12 Gyr in the local universe. Eales et al. (2017) plotted the galaxy mass versus the specific SFR (SSFR; their Figure 2, the Galaxy Main Sequence) showing that LTGs and ETGs form a sequence with negative slope without any distinct separation between LTGs and ETGs. They concluded that a rapid quenching process is not required. A more gentle process, which they called "slow quenching," better describes the observations. In other words, SF properties change gradually, accompanied by morphological transformations. The evolution that comes out of our SPH-CPI simulations is consistent with this picture. Quenching is faster in the more massive systems (see Figure 8). Looking at Figure 7 and Table 4, we show that the merger (defined in Section 4) occurred at redshift $\geqslant 1$ for the large majority of our sample (84% of the larger sample considered, or 91%, 10 out of 11 here), and that these galaxies assembled almost all of their stellar mass from the merger event to the present. Therefore, our galaxies evolve in a rather different way from the assumption by Weigel et al. (2017), which investigated the process of major merger quenching and its importance at $z \leqslant 0.5$. Our SPH-CPI simulations indeed show that while transitioning from the merger to the red early-type stage, galaxies gain significant amounts of their stellar mass, at odds with the Weigel et al. (2017) assumption. Their analysis suggests that major mergers are likely to lead to an evolution from star-forming to quiescent galaxies via quenching. However, they specified that it is unlikely that major mergers account for the majority of the quenching expected within the last 5 Gyr. They further conjectured the existence of alternative quenching channels to explain the existence of the GV and RS population, which are likely to lead to a slow GV transition. Our SPH-CPI simulations suggest that mergers and interactions are important

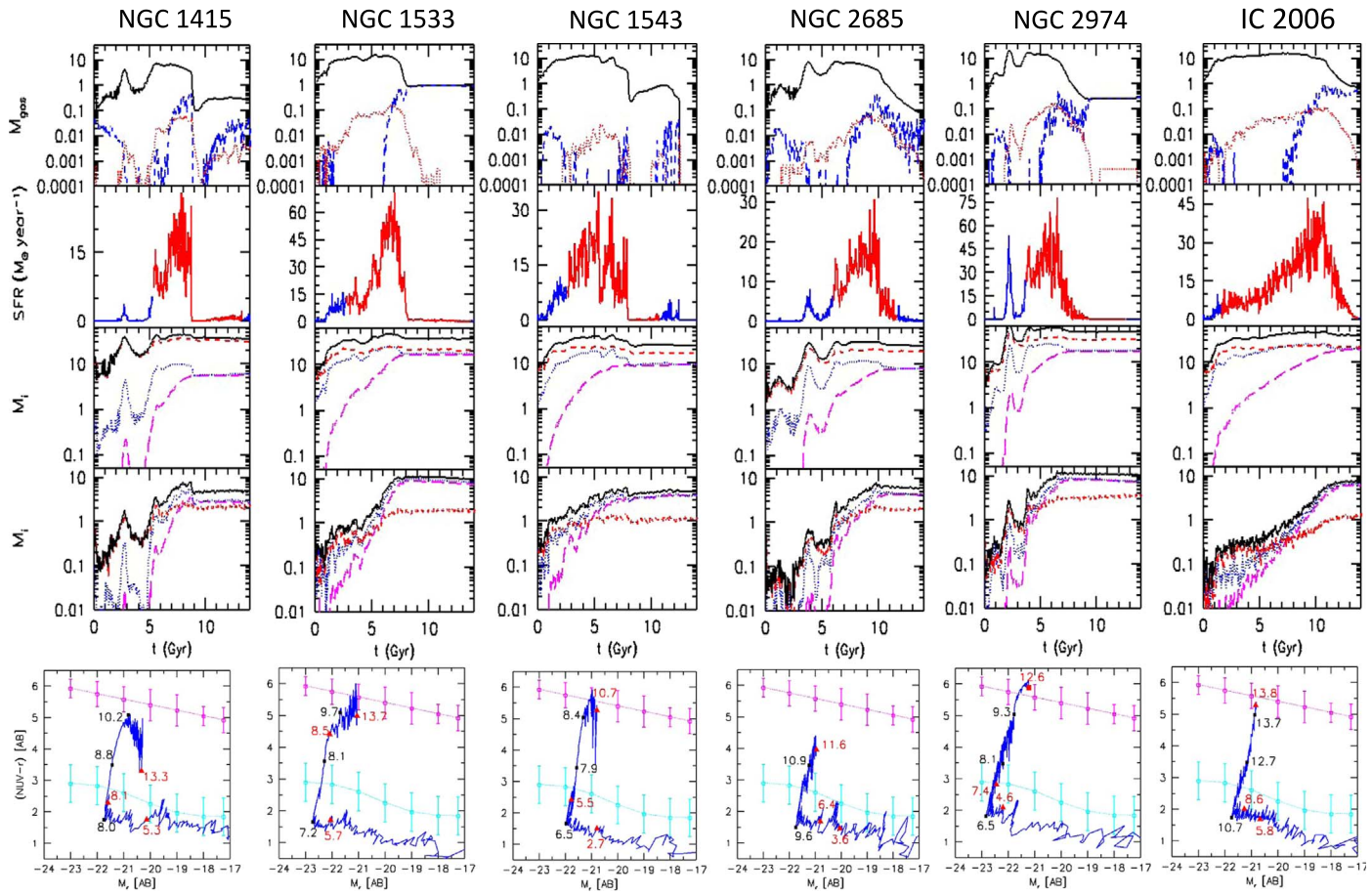

Figure 5. Same as Figure 4 but for ETGs with UV features.

Table 3
Properties of 11 ETGs from Simulations

Galaxy	M_B	Age	M_* ($10^{10}\,M_\odot$)		$M_{\rm tot}$ ($10^{10}\,M_\odot$)	
	(mag)	(Gyr)	$M_{R_{25}}$	M_{50}	$M_{R_{25}}$	M_{50}
(1)	(2)	(3)	(4)	(5)	(6)	(7)
NGC 1366	−18.65	11.1	1.49	3.68	2.06	16.83
NGC 1415	−19.30	13.3	2.52	5.39	4.99	36.10
NGC 1426	−19.42	13.0	3.75	9.22	5.79	28.73
NGC 1533	−19.90	13.7	7.16	15.85	10.64	36.65
NGC 1543	−19.70	10.7	3.35	8.60	4.56	25.70
NGC 2685	−19.72	11.6	4.05	7.47	6.21	26.34
NGC 2974	−19.92	12.6	6.90	16.71	10.47	47.45
NGC 3818	−20.42	13.5	9.88	21.38	15.01	51.99
NGC 3962	−21.24	9.6	8.07	24.43	28.21	61.23
NGC 7192	−20.52	12.5	11.80	19.95	17.82	52.84
IC 2066	−19.75	13.8	5.90	18.07	7.68	39.26

Note. The intrinsic total B-band absolute magnitude is in column 2; the galaxy age is in column 3; the stellar mass derived within our selected reference radii, R_{25} (Table 1), and 50 kpc are in columns 4 and 5; and the corresponding total mass is in columns 6 and 7.

mechanisms to drive galaxy transformations, and that SF quenching due to gas exhaustion and SN feedback several gigayears after the merger/encounter occurred is enough for galaxies in low-density environments. Moreover, quenching, which drives the crossing of the GV, depends on the galaxy mass (Figure 8, left). No alternative/additional quenching channels are required other than the gas exhaustion by SF and stellar feedback.

Cosmological simulations have shown that AGN feedback is required to reproduce the cosmic SFR, downsizing phenomena, and mass–redshift dependence of the SSFR (Wang et al. 2019, and references therein). At the same time, the cosmological simulations of Taylor & Kobayashi (2015) showed that galaxy evolution in the stellar mass range 9–11 $\log(M_\odot)$ is almost unaffected by AGN/black hole feedback. Semi-analytic simulations by Henriques et al. (2019) that included AGN feedback also found that SNe dominate galaxy quenching in their intermediate-mass halo regime. Hydrodynamical simulations by Katsianis et al. (2017, EAGLE project) claim that SN feedback is important at all redshifts and plays a major role in reproducing the observed number density of star-forming galaxies at all epochs. All of these works point out the role of SN feedback in galaxy quenching and thus in galaxy transformation. We also emphasize that, in the range of total mass 10.4–11.8 $\log(M_\odot)$ and galaxy stellar mass 9.5–11.4 $\log(M_\odot)$, more massive galaxies are quenched faster than less massive ones, because gas is more rapidly transformed in stars, and SNe feedback is also enhanced. As a consequence, brighter, more massive galaxies spent a shorter time in the GV than fainter, less massive ones (Mazzei et al. 2014b). The galaxy transformation to ETGs is faster in more massive galaxies. The quenching process is, however, a gentle process, lasting more than 1 Gyr, as we found in NGC 3818, the most massive galaxy by-product of a major merger we analyzed. Our

Table 4
Percentages of the Stellar Mass Growth in Different Evolutionary Time/Redshift Intervals

Galaxy	Δz(1–0)		Δz(0.5–0)		Δz(BP–0)		Δz(GV)		Δz(GV–0)	
	%		%		%		%		%	
NGC 1366	87.1	96.3	31.7	52.4	18.9	14.1	3.1	12.0	3.4	10.3
NGC 1415	87.0	94.9	18.8	−3.2	21.7	0.7	−1.2	−4.2	1.6	−12.0
NGC 1426	59.0	79.4	16.7	34.6	31.5	53.0	3.8	9.4	4.3	11.0
NGC 1533	60.3	86.8	0.5	−17.8	11.3	11.7	−0.9	−3.8	0.7	−18.8
NGC 1543	85.4	89.3	27.9	49.0	8.0	17.4	−6.4	−2.9	−2.1	−2.9
NGC 2685	92.5	99.6	71.9	94.0	15.9	18.1	1.6	−0.7	1.6	−0.7
NGC 2974	62.4	81.5	2.73	7.34	14.1	1.6	0.9	−1.0	0.5	−14.9
NGC 3818	78.7	93.4	39.6	58.6	−4.9	−36.5	−1.9	−0.7	−3.0	−8.5
NGC 3962	98.2	99.2	82.9	91.2	12.3	11.3	1.1	4.5	1.3	4.1
NGC 7192	82.7	94.3	57.4	79.6	3.8	0.2	1.5	6.4	1.8	4.1
IC 2066	80.5	97.9	52.4	88.9	10.3	37.3	0.7	−2.3	0.9	−0.11

Note. Percentages within 50 kpc are on the left, while those within R_{25} (Table 1) are on the right. NB: the negative fractions indicate mass loss in the interval considered.

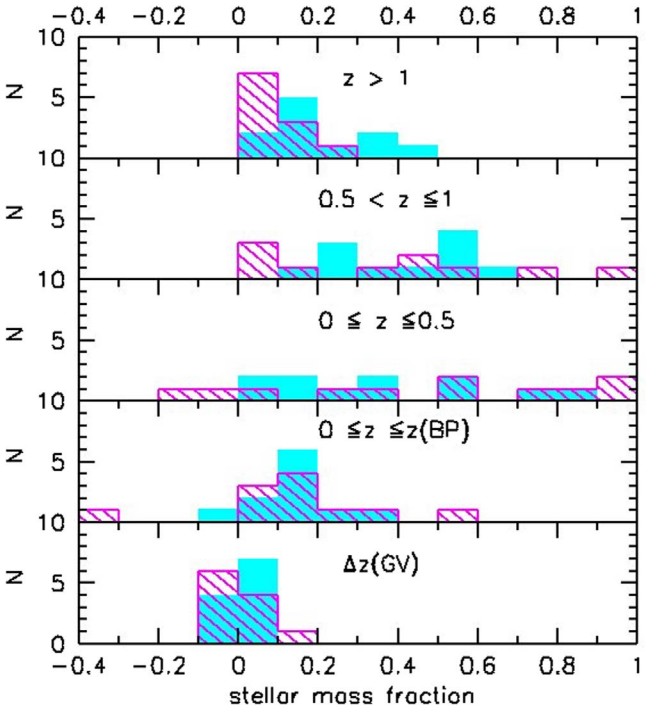

Figure 6. Number of galaxies vs. fraction of stellar mass assembled in different evolutionary steps within 50 kpc (cyan regions) filled and R_{25} in Table 1 (magenta hatched regions). Accounting for the cosmological parameters in Section 1, the look-back times to redshift 0.5 and 1 are about 5.2 and 8 Gyr, respectively; BP and GV indicate the BP and the GV of the CMD of each galaxy. NB: the negative fractions indicate mass loss in the interval considered.

findings are consistent with the results of Genzel et al. (2014). Their percentage of galaxies with AGN at $z > 1$ and $\log M > 10.9\,M_{\odot}$ is about 30%. The mass built up to $z > 1$ of our simulated galaxies is, on average, less than 20% of their galaxy mass at $z = 0$ (Table 3). Only two systems have in place more than 40% at $z > 1$ (Table 4). Therefore, the galaxy stellar masses of our targets at $z > 1$ are all below the threshold mass of Genzel et al. (2014).

Our conclusions are based on the results of the SPH-CPI simulations best describing the current properties of 19 ETGs in nearby groups. The evolutionary picture we present agrees with the recent findings by Eales et al. (2017), not only for the discussion above concerning quenching length but also because several ETGs analyzed here are not "dead" at $z \leqslant 0.5$, as the authors themselves claimed (Eales et al. 2018a, 2018b). Our simulations show that the percentage of stellar mass assembled within this redshift range varies considerably from about 80% to less than 1%. The stellar mass gained while crossing the GV is, however, always very small, $\leqslant$4% (Table 4).

6. Conclusions

We use SPH-CPI simulations anchored to the global properties of 11 ETGs located in low-density environments to shed light on both the mechanisms at the origin of their UV features, if any, and their evolution. All of the simulations start from collapsing triaxial systems composed of DM and gas. We find that there are no significant differences in the formation mechanisms between ETGs with or without UV features. Major as well as minor mergers can trigger evolutionary phases characterized by the appearance of UV features sometimes extending up to the galaxy outskirts, as observed. In both cases, the UV morphology is long-lasting. In minor mergers such as NGC 1415 and NGC 1543, each UV feature observed survives for less than 0.5 Gyr, on average. However, the UV emission is characterized by features that form with continuity from the beginning of the merger to its current age, so that the overall morphology lasts 8.1 Gyr. In major mergers, the resulting UV features last several gigayears; one of these features is the inner ring of NGC 1533. Simulations of galaxy encounters with a small companion match well the properties of normal ETGs. Our set of galaxies spans a large range of ages, between 9.6 and 13.8 Gyr, and total stellar masses, from 3.7 to 24.4 $\times$ $10^{10}\,M_{\odot}$, with the most massive, NGC 3962, also being the youngest.

Our simulations, which include stellar feedback from SNe, show that the gas accretion history self-regulates the SFR that drives the galaxy evolution without the need to invoke any external or additional (e.g., AGN) quenching, as shown in Figures 4 and 5, in agreement with the observing pictures of Bremer et al. (2018) and Eales et al. (2017, 2018a, 2018b). Simulations by Taylor & Kobayashi (2015), EAGLE hydrodynamical simulations by Katsianis et al. (2017), and recent results of semi-analytical simulations by Henriques et al. (2019) all outline the importance of SN feedback in driving the galaxy quenching in suitable mass ranges. Our results suggest that the AGN does not affect the general/global evolution (shown in Figures 4 and 5) of our targets. However, AGN

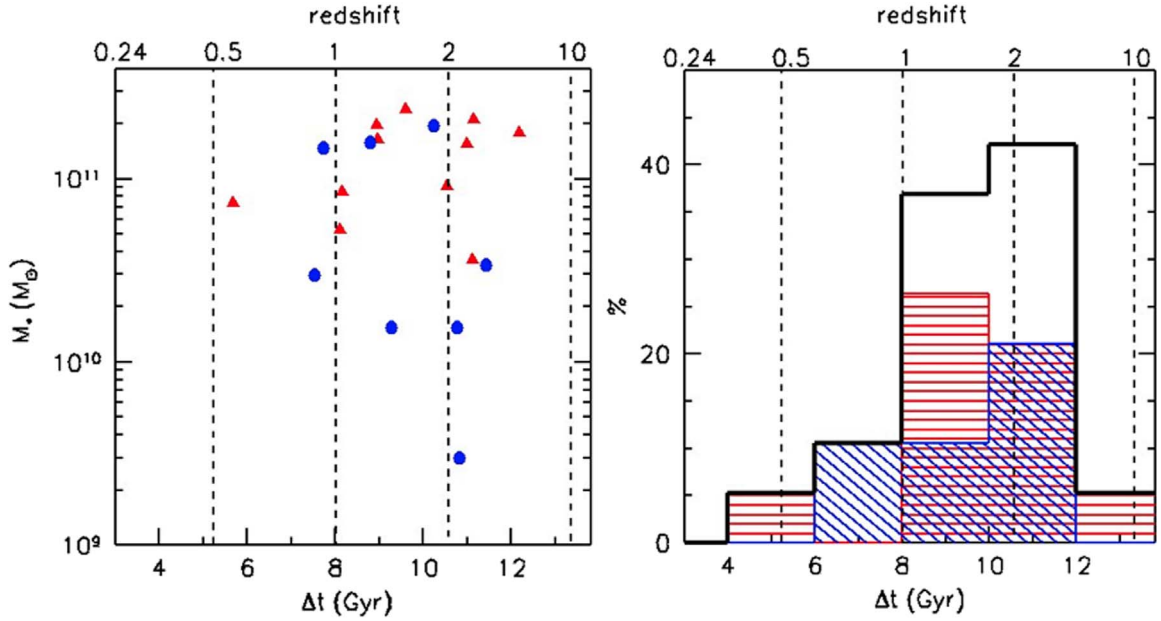

Figure 7. (Left) Total stellar mass at $z = 0$ vs. age (either merger age or time of the onset of the SF due to galaxy flyby). The merger age (Δt) is the difference between the galaxy age at $z = 0$ and that at the beginning of the merger (Section 4). Red triangles are the 11 galaxies studied in this paper, and blue circles are the eight galaxies from Mazzei et al. (2014a). (Right) Histogram of the percentage of ETGs as a function of age (again, either merger age or time of the onset of the SF due to galaxy flyby). The horizontally shaded histogram is for galaxies in this paper, while the diagonal one is for those in Mazzei et al. (2014a), both normalized to the total number of ETGs analyzed (19; thick line).

feedback could be important in the nuclear regions at scales below those we have considered here (50 pc).

The quenching is mass-dependent. Brighter, more massive galaxies spend a shorter time in the GV than fainter, less massive ones. Both of these conclusions are based on the results of the SPH-CPI simulations presented here, anchored to the current properties of 11+8 ETGs in nearby groups, whose stellar mass range, 0.3–24.4 ($10^{10}\,M_\odot$), is about 2 orders of magnitude. We plan to extend our work to a large number of ETGs, both to better sample this stellar mass range and/or to expand it.

The DM mass always exceeds the stellar mass within the larger radius we analyzed, 50 kpc, and their ratio tends to a constant value as the SF quenches. The opposite behavior occurs within the smaller radius, equal to the current value of R_{25}, for which the stellar mass exceeds the DM one as the SF quenches. Mergers and/or interactions enhance the SF, which proceeds differently from the case of a single, isolated galaxy (Mazzei & Curir 2003), since these mechanisms deepen/modify the potential well where the gas is accreting. The growth of the stellar mass develops from the SF driven by this accretion history. A large amount ($\geqslant$50%) of the current stellar mass of each galaxy is still assembling at redshift $\leqslant$0.5 for 35% of our sample and would give a significant contribution to the IR-bright galaxy population detected by the *Herschel* (Eales et al. 2017, 2018a, 2018b), *Infrared Space Observatory* (*ISO*), and *IRAS* satellites (Mazzei et al. 2007) before the complete morphological, dynamic, and photometric transformation toward ETGs.

We acknowledge use of the HyperLeda database (http://leda.univ-lyon1.fr) and the NASA/IPAC Extragalactic Database (NED), which is operated by the Jet Propulsion Laboratory, California Institute of Technology, under contract with the National Aeronautics and Space Administration. P.M. and R.R. acknowledge funding from PRIN-INAF SKA 2017 program 1.05.01.88.04. We thank the referee for helpful comments that helped improve our manuscript.

Appendix A
ETGs without UV Features

The galaxies NGC 1366, NGC 1426, NGC 3818, NGC 3962, and NGC 7192 have no peculiar morphological features in their optical and UV images (Figure 2 and Paper II).

A.1. NGC 1366

The simulation that best describes the global properties of this galaxy corresponds to an encounter between two counter-rotating halos with a mass ratio of 10:1, our target being the more massive one (Table 2). The snapshot that matches the global properties of this S0 galaxy (Paper II) gives $M_B = -18.65$ mag (compare with Table 1) at a galactic age of 11.1 Gyr. At this time, the companion galaxy lies 656 kpc away from our target, about 107′ on the plane of the sky using the cosmological parameters in Section 1. Their closest approach occurred 5.9 Gyr earlier, when our target was 5.2 Gyr old, at $z = 0.61$. The galaxy age estimated by averaging those of the stellar populations at the best-fit snapshot is 7 Gyr, or 5.7 Gyr when weighting these ages by *B*-band luminosity. These estimates agree well with the 5.9 ± 1 Gyr of Annibali et al. (2007). Figure 1 shows the good match over almost 4 orders of magnitude in wavelength between the snapshot SED (red solid line) and the observations. Magenta points are from S4G[5] and yellow points from the *WISE* catalog.

The shape of the FIR SED is that expected, on average, for ETGs (Mazzei et al. 1994; Mazzei & De Zotti 1994) with a warm-to-cold dust ratio of 0.05 and a cutoff radius of the cold dust distribution $r_d = 3$ kpc. Moreover, the FIR–to–*B*-band

[5] The Spitzer Survey of Stellar Structure in Galaxies (S4G), IRAC's 3.6 and 4.5 μm channels: https://irsa.ipac.caltech.edu/data/SPITZER/S4G/.

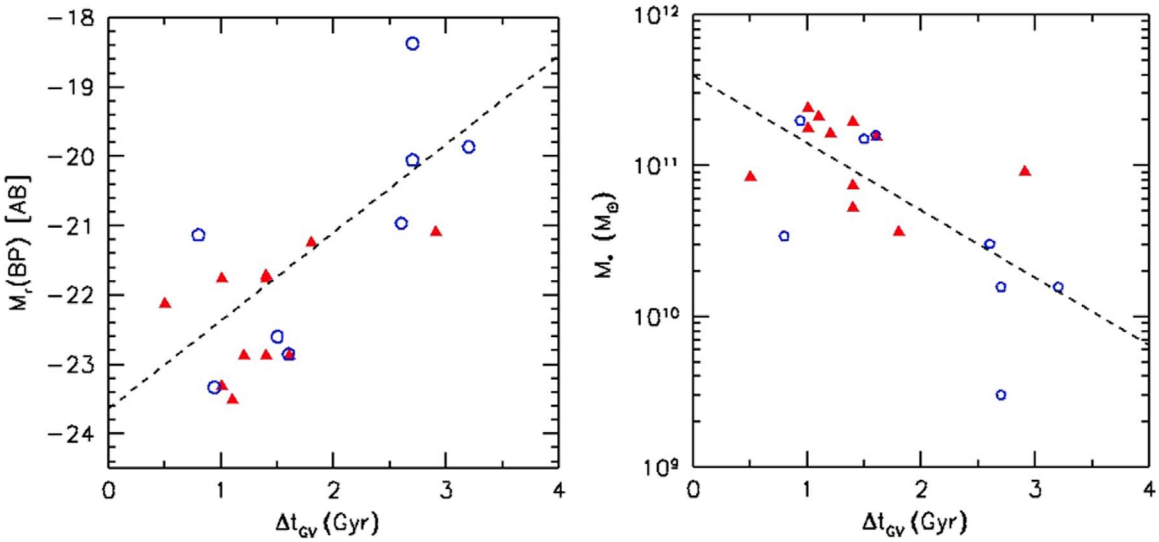

Figure 8. (Left) Absolute M_r magnitude reached at the BP of the rest-frame CMD vs. time spent in the GV, as defined in Section 4. The correlation (dashed line) index is 0.72, and the slope of the regression is 1.27. (Right) Total stellar mass at $z = 0$ vs. time spent in the GV. The correlation (dashed line) index is −0.67, and the slope of the regression is −0.45. Symbols are the same as in Figure 7.

luminosity ratio, 0.02, agrees well with the value-expected, on average (Mazzei & De Zotti 1994), and the FIR luminosity is 8% of the bolometric luminosity. Figures 2 and 3 show the good agreement of morphologies and luminosity profiles. The X-ray luminosity from hot gas at this age, 6×10^{37} erg s^{-1}, and the amount of cold gas (Figure 4, top panel) agree with the upper limits in Table 1. The central velocity dispersion, 115 km s^{-1}, fits well the value of 113.9 ± 3.8 km s^{-1} (HyperLeda catalog), and the maximum stellar rotation velocity, 107 km s^{-1}, agrees well with the value in Table 2 of Paper I (114 ± 19 km s^{-1}). Looking at Figure 4, the DM exceeds the baryonic mass within the larger radius. Their mass ratio sets to a constant value, about 3.5, starting from a galaxy age of 7.6 Gyr. However, within the smaller radius, the stellar mass exceeds the DM by redshift 0.55, corresponding to a galaxy age of 5.5 Gyr. The stellar-to-DM mass ratio sets to a constant, ≈3, starting from 8 Gyr. At this age, the galaxy is leaving the BC to cross the GV in its rest-frame CMD (Figure 4, bottom). Table 4 shows that this galaxy assembles 87% and 32% of its current stellar mass from redshift 1 and 0.5, respectively, but only 3.4% in the past 3.3 Gyr, that is, from $z = 0.27$, within 50 kpc. In the same time/redshift steps, the percentage of stellar mass growth is higher within the smaller radius, given the smaller stellar mass included (Table 4).

A.1.1. NGC 1426

The simulation that matches the global properties of this elliptical is a major merger (Table 2) that begins 2.5 Gyr after the onset of the SFR (Section 4). The best snapshot corresponds to a galactic age of 13 Gyr and $M_B = -19.42$ mag. The age of the galaxy is 9 Gyr by averaging the ages of its stellar populations and 7 Gyr by weighting these ages by B-band luminosity (Table 3). These estimates are in agreement with the value of 9.0 ± 2.5 Gyr by Annibali et al. (2007). Figure 1 compares the observed SED with that provided in Table 3. In the UV spectral range, blue filled circles are *GALEX* from Marino et al. (2011b), yellow points are from Hodges-Kluck & Bregman (2014), and, in the FIR spectral range, magenta points are from Temi et al. (2009). The FIR luminosity accounts for only 0.4% of the bolometric luminosity. The shape of the FIR SED is that expected, on average, for ETGs (Mazzei et al. 1994; Mazzei & De Zotti 1994), with a warm-to-cold dust ratio of 0.5 and a cutoff radius of the cold dust distribution, r_d, of 3 kpc. The X-ray luminosity from hot gas, 2×10^{37} erg s^{-1}, agrees with the upper limit in Table 1. Both the central velocity dispersion, 132 km s^{-1}, and the maximum stellar rotation velocity, 97 km s^{-1}, are consistent with the values in the HyperLeda catalog, 146.7 ± 1.9 and 114 ± 19.0 km s^{-1}, respectively. Looking at Figure 4, the DM exceeds the baryonic mass within 50 kpc (left), and their mass ratio sets a constant value, about 2.2, from a galaxy age of 9.4 Gyr. However, within R_{25} (right), the stellar mass exceeds the DM one by redshift 0.75, corresponding to a look-back time of 6.8 Gyr (i.e., a galaxy age of 6.2 Gyr). The stellar-to-DM mass ratio stays constant, at ≈2, starting from a galaxy age of 9.7 Gyr. This simulation assembles about 59% and 17% of its stellar mass from $z = 1$ and 0.5, respectively, considering 50 kpc (Table 4), and no more than 4% by crossing the GV, accounting for several oscillations. The galaxy spends 6.3 Gyr from the maximum value of its SFR, that is, the BP point of its CMD, and the following quenching ($z = 0$) assembling 31.5% of its stellar mass within the same radius (Table 4).

A.2. NGC 3818

The simulation that best describes the global properties of this E galaxy is a major merger (Table 2). The best snapshot representing the global properties corresponds to a galaxy age of 13.5 Gyr with a B-band absolute magnitude of −20.42 mag (Table 3). The age of the galaxy becomes 8 Gyr by averaging those of its stellar populations and reduces to 6.3 Gyr by weighing these ages by B-band luminosity (Table 3). These estimates agree with Annibali et al. (2007), who gave 8.8 ± 1.2 Gyr for this galaxy. Figures 1–3 compare the observed and simulated properties. The blue filled circles in the UV spectral range are *GALEX* data from Marino et al. (2011b), and the black dots are from Hodges-Kluck & Bregman (2014). The FIR SED, not strongly constrained by the observations, corresponds to a FIR-to-bolometric luminosity ratio

of 0.008 and a FIR-to-blue luminosity ratio of 0.005, in agreement with findings by Mazzei & De Zotti (1994) for a complete sample of Es. The X-ray luminosity of the hot gas expected at the best-fit age agrees with that in Table 1, being $\simeq 2 \times 10^{39}$ erg s^{-1}. Both the maximum velocity of the stars, 99 km s^{-1}, and their central dispersion velocity, 180.3 km^{-1}, are in good agreement with observational constraints (Paper I, their Table 2) in the HyperLeda catalog (106.7 ± 14.8 and 193.4 ± 3.7 km s^{-1}, respectively). Figure 4 shows that the SFR provided by this simulation reaches the highest value, 168 $M_\odot$ yr^{-1}, for all simulations presented here. Therefore, is it not surprising that the residual SFR cannot compensate for the death rate during crossing of the GV (Table 4). The galaxy moves along the BC of its rest-frame CMD until reaching its highest SF and brightest magnitude when the galaxy is 9.2 Gyr old. Then, the SF quenches by itself due to the gas ejection and exhaustion produced by its high regime. When the SF is stopped, the stellar mass assembly becomes negative (Table 4). The percentage of its current stellar mass assembled from redshift 1 is 79%, and $z = 0.5$ is 40%, within 50 kpc (Table 4). The DM exceeds the stellar mass within this radius along all of the evolution. Their mass ratio reaches a constant value, $\simeq$1.4, starting from about 10 Gyr. Looking at the smaller fixed radius, R_{25}, in Table 1 (Figure 4), about 35% of the current stellar mass is assembled between redshift 1 and 0.5 and $\simeq$59% between 0.5 and zero. The stellar mass exceeds the DM one starting from 8.4 Gyr, and their mass ratio becomes almost constant (2) starting from 9.6 Gyr, that is, in the GV.

A.3. NGC 3962

This elliptical (E1) galaxy is a particularly intriguing case. Our UV structural analysis (Paper II) does not give any clear evidence of a disk; however, signatures of some recent SF have been detected (e.g., Paper II). Moreover, this system entails a large amount of both cold and hot gas (Table 1). The simulation that best reproduces the global properties of this galaxy corresponds to a flyby between two halos with a mass ratio of 10:1 (Table 2), our target being the more massive one. From the snapshot selected, the galaxy age is 9.6 Gyr and the B-band absolute magnitude is $M_B = -21.2$ mag (Table 3). At this time, the companion galaxy lies 513 kpc away from our target, about 50′ in projection on the sky. The closest approach, 507 kpc, between the two galaxies is realized 0.37 Gyr after the best snapshot. The age of the galaxy, estimated by averaging the ages of its stellar populations, is 4 Gyr and reduces to 3.2 Gyr by weighing the ages by B-band luminosity within R_{25}. Annibali et al. (2007) estimated 10.0 ± 1.2 Gyr for this galaxy, whereas Serra & Oosterloo (2010) gave $2.5^{+0.4}_{-0.3}$ Gyr. This value is in good agreement with the central age (within 1 kpc) we derive by weighing the ages of the stellar population by B-band luminosity, that is, 2 Gyr. Figure 1 shows the match of the SED from the best snapshot with the observed data. Blue filled circles in the UV range are *GALEX* data from Marino et al. (2011b); in the FIR spectral range, magenta symbols are *ISO* observations from Temi et al. (2004, 2009); and yellow triangles are MIPS and SCUBA upper limits at 450 and 800 μm from Leeuw et al. (2004). The FIR SED entails about 9% of the bolometric luminosity. The diffuse radiation due to cold dust corresponds to a disk distribution of dust and stars with a central intensity of double that in our own Galaxy (Mazzei et al. 1992). The warm dust component requires a temperature of 48.5 K instead of 62 K in the Milky Way, as well as a warm/cold luminosity ratio of 0.5. The H_α observations by Zeilinger et al. (1996) highlighted the presence of a inner disk with a radius of about 1 kpc (5″) and a brighter armlike feature extending up to 3.4 kpc (20″). Unfortunately, neither *GALEX* (Marino et al. 2011a) nor *Swift* (Paper II) detected UV features associated with this emission. This simulation provides a gas amount in agreement with the value in Table 1 (Figure 4). This gas concentrates in the inner 4 kpc, in good agreement with findings by Zeilinger et al. (1996). Moreover, its maximum rotation velocity, 110 km s^{-1}, agrees with the value provided by the HyperLeda database (99.1 ± 7.7 km s^{-1}), as well as the central ($r \leqslant 1$ kpc) velocity dispersion of stars, 220.6 km s^{-1}, comparable to 220.3 ± 12.6 km s^{-1}. The X-ray luminosity of the hot gas expected at this age is $\simeq 1.5 \times 10^{39}$ erg s^{-1}, about half that in Table 1. Figure 4 shows that the DM always exceeds the stellar mass within 50 kpc. Their mass ratio is constant, 1.5, starting from 8.4 Gyr. However, within the smaller radius, R_{25}, the stellar mass exceeds the DM one from 6.8 Gyr, and their mass ratio becomes constant, 1.8, from 8.4 Gyr again, when the galaxy is moving in the GV. Following this simulation, the galaxy lives on the BC, 7.4 Gyr, until it reaches its brightest magnitude. Then, the SFR quenches by itself due to the gas exhaustion produced by its high regime and related feedback in about 0.8 Gyr, leading the galaxy out of the BC. The galaxy crosses the GV in 1 Gyr, accounting for some percent of its final stellar mass assembly within both our reference radii (Table 4).

A.4. NGC 7192

The simulation that best fits the global properties of NGC 7192 is a major merger (Table 2). The galaxies merge 3.6 Gyr after the onset of the SF. The snapshot that matches the global properties of this galaxy provides a galaxy age of 12.5 Gyr and $M_B = -20.5$ mag (compare with Table 3). By averaging the age of its stellar populations, we derive 7 and $\simeq$5 Gyr by weighing these ages by B-band luminosity, in good agreement with Marino et al. (2011a, and references therein). In Figure 1, which compares the observed SED with that from the selected snapshot, the blue filled circles in the UV spectral range are *GALEX* data from Marino et al. (2011b). Comparisons of morphologies and luminosity profiles are in Figures 2 and 3. The FIR SED is that described in Mazzei et al. (1994), with, however, a warm/cold dust ratio, $r_{w/c} = 0.05$. The FIR luminosity is equal to 3.6% of the (intrinsic) bolometric luminosity, and the FIR-to-blue luminosity ratio is 0.009, in agreement with the results of Mazzei & De Zotti (1994). The amount of cold gas in Table 1 agrees with the results from the selected snapshot, although a larger gas reservoir is expected from this simulation (Figure 4, top). Both the central velocity dispersion, 171 km s^{-1}, and the rotation velocity of the stars, $\leqslant$20 km s^{-1}, agree with the observational constraints, 177 ± 5.4 and 0 km s^{-1}, respectively, from the HyperLeda catalog. By exploiting *Spitzer* IR spectra, Rampazzo et al. (2013) found PAH signatures in the inner region of this system, pointing at an active stage of SF in the past 2 Gyr, in agreement with the evolutionary picture highlighted in the CMD of Figure 4 (bottom panel). Moreover, they also emphasized a possible nonthermal contribution due to LINER activity. Our simulation provides an X-ray luminosity of the hot gas in this system five times lower than in Table 1. The DM mass always exceeds the stellar mass within 50 kpc. Their mass ratio becomes constant, 1.7, from 10.7 Gyr, when the galaxy lies in the GV. The percentages of stellar mass assembled from redshifts 1 and 0.5 are about 83% and 57%, respectively (Table 4). Looking

within the smaller radius, R_{25}, in Table 1, the stellar mass dominates the DM starting from ≈8 Gyr, corresponding to a look-back time of 4.6 Gyr ($z = 0.42$; Section 1). Their ratio sets on a constant value, 2, from an age of 10.4 Gyr. Of the current stellar mass, 94% is assembled from redshift 1 and ≈80% from 0.5 within this radius (Table 4). This galaxy lies on the BC 10 Gyr, taking only 0.3 Gyr to get out. Then, it crosses the GV in 1.4 Gyr, attaining its actual position in 2.2 Gyr. The stellar mass assembled within 50 kpc during this route, that is, from the GV to $z = 0$, is only 1.8% of its current mass and 4.1% within R_{25} (Table 4).

Appendix B
ETGs Showing UV Ring/Armlike Features

The galaxies NGC 1415, NGC 1533, NGC 1543, NGC 2685, NGC 2974, and IC 2006 show UV features (Figure 2). We point out that Sérsic functions (blue lines in Figure 3) cannot account for these features, which indeed appear in the UV luminosity profiles of simulations (red lines).

B.1. NGC 1415

The global properties of this galaxy are well matched by a minor merger (Table 2). Following this simulation, NGC 1415 is 13.3 Gyr old, with $M_B = -19.3$ mag (compare with Table 1). By averaging the age of its stellar populations, we estimate 8 and 5.3 Gyr by weighing the same ages by *B*-band luminosity. The blue filled circles in the UV range of Figure 1 are *GALEX* FUV from Buat et al. (2007), the higher fluxes in the near-IR range are from Spinoglio et al. (1995), and the yellow data in the FIR spectral range come from the *AKARI* FIS catalog. The FIR SED requires a warm-to-cold luminosity ratio, $r_{w/c}$, of 1.2, more than twice as much as expected, on average (Mazzei & De Zotti 1994). Moreover, 74% of the intrinsic bolometric luminosity of this galaxy comes out in the FIR spectral range. These points contradict its classification as an ETG, enforcing that of an LTG (SB; see Table 1 in Paper II and Section 2). The amount of cold gas and the X-ray luminosity of the hot gas in Table 1 agree well with the results from the selected snapshot, $1.8 \times 10^9 M_\odot$ and 2×10^{39} erg s^{-1}, respectively. Moreover, the maximum rotation velocity of cold gas, 168 km s^{-1}, is like the value in the HyperLeda catalog (163.6 ± 6.1 km s^{-1}).

Figure 5 highlights the evolutionary properties of the selected simulation. The merger begins (Section 4) after 5.2 Gyr ($z = 1.03$) from the onset of the SFR. Looking at the evolution of the different mass components within the reference radii in Section 4, a large percentage of the current stellar mass is assembled from redshift 1 within both of these radii (Table 4). The stellar mass becomes equal to the DM one within R_{25} at redshift 0.52; their mass ratio, 1.23, is almost constant from $z = 0.42$ to zero, that is, from 8.7 Gyr. However, the DM mass always exceeds the stellar mass within the larger radius, 50 kpc. Their mass ratio becomes constant, about 6.2, starting from a galaxy age of about 9 Gyr. This galaxy lies in the BC for 8 Gyr, taking about 0.8 Gyr to cross it, and reaches the RS at an age of 10.1 Gyr. Its SFR turns off for about 1 Gyr while the galaxy is crossing the GV. From this shutdown arises the negative fraction of stellar mass assembled during this phase (Table 4). Then, the system goes back to the GV, where it stays the last 2 Gyr until it reaches its current position at 13.3 Gyr.

This simulation points out that the GV is not only a transition zone but also a region where some ETGs can come back to live for several more gigayears.

B.2. NGC 1533

Mazzei et al. (2014b) already studied this galaxy, matching some of its global properties—absolute magnitude, SED, *GALEX* UV morphology, and kinematical properties—with a major merger (Table 2) between halos with perpendicular spins. The merger occurs at $z = 2.3$, that is, 2.7 Gyr after the onset of the SF. From the chosen snapshot, they derived that NGC 1533 is 13.7 Gyr old, with $M_B = -19.9$ mag. Here we confirm their results and add new comparisons (see below). In particular, the SED in Figure 1 includes new data from Paper II (green) and the CGS catalog (black). Comparisons of *V* and M2 `Swift-UVOT` images (Figure 2), as well as their luminosity profiles (Figure 3), are not in the previously cited paper. The X-ray luminosity provided by the hot gas at this age is well below the upper limit in Table 1. According to this simulation, the UV ring is a resonance feature in the evolutionary scenario of this galaxy. The ring arises when the galaxy is about 8 Gyr old, corresponding to $z \simeq 0.57$ using the cosmological parameters in Section 1. Looking at Figure 5, the DM mass exceeds the stellar mass within 50 kpc by a factor that becomes almost constant at 1.26 after 8.1 Gyr. However, within the smaller radius, the stellar mass dominates on the DM starting from 5.3 Gyr. The mass ratio becomes constant (≃4) after 8.1 Gyr from the SF onset. This system lies on the BC for 7.2 Gyr, takes about 0.9 Gyr to cross it, and gets to the RS in 1.6 Gyr, reaching its current position after 4 Gyr. This galaxy enters the GV at a redshift higher than 0.5, the only case in our sample. Table 4 shows that 40% of its current stellar mass is assembled before redshift 1 and only 0.5% from 0.5 to zero. Moreover, the percentage assembled moving from the brightest to the actual location in its CMD, that is, during the SF quenching, is 11%.

B.3. NGC 1543

This galaxy results from a minor merger (Table 2). From the snapshot that matches its global properties, NGC 1543 is 10.7 Gyr old, with $M_B = -19.7$ mag. By averaging the age of its stellar populations, we derive 6.5 and 5.6 Gyr by weighing the same ages by *B*-band luminosity within a radius of 50 kpc. The SED is well matched by the selected snapshot (Figure 1). The blue data in the FIR range are from Temi et al. (2009). The shape of the FIR SED is that expected for ETGs (Mazzei et al. 1994); however, it requires a warm/cold dust ratio of 0.05. The FIR luminosity is 5% of the intrinsic bolometric luminosity and 1% of the *B* luminosity ratio. The amount of cold gas and the X-ray luminosity in Table 1 agree well with our results, $7.8 \times 10^8 M_\odot$ and 1.7×10^{38} erg s^{-1}, respectively. The average rotation velocity of the stars, 71.4 km s^{-1}, and their central velocity dispersion, 157 km s^{-1}, agree well with the values in the HyperLeda catalog (70.7 ± 14.4 and 149.4 ± 4.4 km s^{-1}, respectively). Looking at its evolutionary properties (Figure 5), we note that the DM mass always exceeds the stellar one within the larger radius (50 kpc). Their mass ratio becomes a constant, ≈1.8, starting from an age of about 8.4 Gyr ($z = 0.18$). From this point to $z = 0$, about 4.4% of the stellar mass is assembled (Table 4). A large percentage of the current stellar mass (85%)

is assembled from redshift 1 and 28% from 0.5. Moreover, the percentage assembled by moving from the BP to its actual location in the CMD, that is, during the quenching of the SFR, is 8% (Table 4). However, the SFR cannot compensate for the stellar death rate during the crossing of the GV, so the stellar mass growth is negative within this radius. Looking at the smaller radius, R_{25}, the stellar mass exceeds the DM one starting from a galaxy age of 4.4 Gyr, corresponding to a look-back time of 6.3 Gyr ($z = 0.66$). Then, the stellar-to-DM mass ratio sets to a constant value, ≈3, from the entry in the RS to $z = 0$. The stellar mass assembly history provides 49% of the current stellar mass from $z = 0.5$% and 16% from the BP of its CMD (Table 4). While crossing the GV, the percentage of stellar mass accreted is negative, −2.9%, due to the quenching of the SF for about 1 Gyr. However, in the last 2.3 Gyr (from $z = 0.18$ to zero), the percentages of current stellar mass assembled become positive within $r = 50$ kpc due to short accretion episodes that produce galaxy rejuvenation, moving back the galaxy in the GV.

B.4. NGC 2685

The simulation that provides the best description of the global properties of NGC 2685 is a major merger between two halos with perpendicular spins (Table 2). From these conditions arises a late merger, occurring about 6 Gyr from the onset of the SF. The snapshot that best matches the global properties of this galaxy gives a galaxy age of 11.6 Gyr and $M_B = -19.7$ mag (Table 3). By averaging the ages of its stellar populations, we derive 6.2 and 3.2 Gyr by weighting the ages by B-band luminosity. The total SED is well matched by the selected snapshot (Figure 1); the cyan squares in the UV wavelength range are GII data from the *GALEX* catalog (DR7), and the black dots are the CModel of SDSS. As in the previous figures, all data have been corrected for galactic extinction, in particular, the *GALEX* data following Marino et al. (2011b). The shape of the FIR SED (Mazzei et al. 1994) requires a warm-to-cold dust ratio of 0.1. The FIR luminosity is about 25% of the intrinsic bolometric luminosity, very unusual for ETGs, and 14 times larger than the B-band luminosity. The amount of gas in Figure 5 and the X-ray luminosity, $\leqslant 0.01 \times 10^{40}$ erg s^{-1}, are in good agreement with observational constraints (Table 1). The central stellar velocity dispersion ($r \leqslant 1$ kpc) is 105 km s^{-1}, in agreement with the value in HyperLeda (98.9 ± 3.6 km s^{-1}), and the stellar rotation velocity, 110.2 km s^{-1}, agrees with the inclination-corrected value (112.4 ± 11.9 km s^{-1}) in the same catalog. By considering the fixed spherical radius of 50 kpc, this galaxy assembles about 92% of its current stellar mass from redshift 1, 72% from redshift 0.5, and only 1.6% while crossing the GV, which corresponds to its current whereabouts (Figure 5 and Table 4). The corresponding fractions within R_{25} (Table 1) are 99%, 94%, and −0.7%. The DM always exceeds the stellar mass within 50 kpc. It becomes $2.5 \times M_{\rm stars}$ in the past 1 Gyr, that is, $z \leqslant 0.075$, but half the stellar mass is within R_{25} in the same redshift range. This galaxy lies on the BC for 9.6 Gyr; it takes about 1.3 Gyr to cross it and an additional 0.7 Gyr to reach its actual position on the GV. The percentages of current stellar mass assembled moving from the BP to the actual location in its rest-frame CMD, that is, during the quenching of the SFR, are 16% and 18% within 50 kpc and R_{25}, respectively.

B.5. NGC 2974

This galaxy is classified as E4 in RC3 but, as discussed in Paper II, the more recent classification is as an SA(r)0/a. A bright near-IR star projected to the SW of its body, BD –03 2751,[6] complicates the picture. The *JHK* magnitudes in NED by Skrutskie et al. (2006) are indeed not the total galaxy magnitudes. We performed a new reduction of the 2MASS images masking the star in order to derive the total galaxy near-IR magnitudes. Following the same method as in Paper II, we derive integrated magnitudes 1.5 mag fainter, although with a large error: $m_J = 8.65 \pm 0.48$, $m_H = 7.99 \pm 0.40$, and $m_K = 7.78 \pm 0.49$. We report these data in Figure 1 with their 2σ errors to describe the SED of this galaxy. A major merger (Table 2) provides the best description of its global properties. The merger occurs 3.7 Gyr after the onset of the SF. The snapshot selected provides $M_B = -19.9$ mag and a galactic age of 12.6 Gyr. The age of the galaxy estimated by averaging the ages of its stellar populations is 9.3 Gyr and reduces to 7.8 Gyr by weighting their ages by B-band luminosity. Annibali et al. (2007) found 13.9 ± 3.61 Gyr for this galaxy. Figure 1 shows the match between the snapshot SED (solid line) and the observed one extended over almost 4 orders of magnitude in wavelength. The near-IR fluxes derived here are shown by filled orange squares. The data in the FIR spectral range are *IRAS* (red), MIPS from Kaneda et al. (2008; green), *ISO* from Temi et al. (2009; magenta), and SCUBA fluxes from Savoy et al. (2009; cyan). The FIR SED accounts for a cold dust component with a central intensity 30% higher than that in Mazzei et al. (1992) and a warm dust component with a temperature half that in our own Galaxy; their ratio is $r_{w/c} = 0.3$. The FIR luminosity is 11% of the bolometric luminosity, one-third of normal disk galaxies (Mazzei et al. 1992). The maximum star rotation velocity at this snapshot, 227 km s^{-1}, agrees with the value in HyperLeda, 211.6 ± 17.3, and that of the gas, 110 km s^{-1}, with 105.2 ± 10.4 km s^{-1} in the same catalog. The amount of cold gas at the best-fit age, $1.1 \times 10^9 M_\odot$ (top panel of Figure 5), is consistent with the value reported in Table 1 accounting for a distance uncertainty corresponding to a mass uncertainty of about 20%. The X-ray luminosity of hot gas at this age, 5×10^{38} erg s^{-1}, is four times lower than the value in Table 1. Looking at Figure 5, the SFR shows a gentle self-quenching after reaching its maximum value due to gas exhaustion and stellar feedback lasting 2.8 Gyr. Then, the SF is, on average, $0.2\,M_\odot$ yr^{-1}, unless the gas reservoir accreted. The DM always exceeds the stellar mass within 50 kpc (middle right) until a stable level is achieved at an age of 7.8 Gyr, that is, for $z \leqslant 0.45$. The DM-to-stellar mass ratio is ≈1.9 in this redshift range. However, within the smaller reference radius, R_{25}, the stellar mass exceeds the DM one from redshift 0.91, that is, a galaxy age of 5 Gyr. Their mass ratio is ≈2 for $z \leqslant 0.5$ (age $\geqslant$ 7.4 Gyr). This galaxy assembles within 50 kpc almost 40% of its current stellar mass at a redshift higher than 1 and only ≈2.7% from 0.5 to redshift 0; the corresponding percentages are about 20% and 7% within R_{25} (Table 4).

B.6. IC 2006

We found that a major merger between two counterrotating halos (Table 2) provides the best match to the global properties

[6] SIMBAD database; http://simbad.u-strasbg.fr/simbad/sim-fid.

of this galaxy. The resulting age is 13.8 Gyr, and $M_B = -19.75$ mag (Table 3). By averaging the age of its stellar populations, we derive 8.1 and 5.2 Gyr by weighing the same ages by B-band luminosity. Annibali et al. (2007) gave 8.1 ± 0.9 for this galaxy. The observed SED in Figure 1 (dots) includes all data reported in its caption and IR fluxes from the SG4 GATOR catalog (magenta triangles). The snapshot selected provides a good match of all these data (solid line). The FIR SED (Mazzei et al. 1994) requires a warm-to-cold dust ratio of 0.05 and a warm dust temperature of about 55 K. The FIR luminosity is 14% of the bolometric luminosity. The amount of cold gas in Table 1 agrees with that provided by the best-fit snapshot, accounting for the minimum temperature available (8400 K), that is, $1.8 \times 10^8\,M_\odot$. The X-ray luminosity of the hot gas is 3×10^{38} erg s^{-1}, somewhat lower than observed. The stellar central velocity dispersion is 140 km s^{-1}, in agreement with Kuntschner (2000; 136 ± 7 km s^{-1}). This galaxy lies on the BC for 12.7 Gyr and takes 1 Gyr to cross the GV, reaching its current position after 1.1 Gyr. The percentages of the current stellar mass assembled within the fixed reference radius of 50 kpc from redshift 1 and 0.5 correspond to 81% and 52%, respectively, and the corresponding fractions within R_{25} are 98% and 89% (Table 4). The percentages of stellar mass assembled moving from the brightest to its actual location, that is, during the quenching of the SFR, are about 10% and 37% within 50 kpc and R_{25}, respectively. The contribution to the stellar mass growth in the GV is only 0.7% within 50 kpc and rises to 0.9%, extending up to $z = 0$; it is −2.3% and −0.1%, respectively, within R_{25}, showing that the SF turns off in the inner regions. The DM mass always exceeds the stellar mass within 50 kpc. However, from an age of 11.5 Gyr, their values become almost the same (their mass ratio is 1.17). Within the smaller radius, R_{25}, in Table 1, the stellar mass exceeds the DM one starting from 7.8 Gyr, and the ratio sets to a constant value, $M_{\rm stars} \approx 4.7 \times M_{\rm DM}$, from the age of about 11.5 Gyr.

ORCID iDs

Paola Mazzei https://orcid.org/0000-0002-8004-1034

References

Annibali, F., Bressan, A., Rampazzo, R., Zeilinger, W., & Danese, L. 2007, A&A, 463, 455
Barnes, J. E., & Hernquist, L. 1996, ApJ, 471, 115
Bettoni, D., Buson, L., Mazzei, P., & Galletta, G. 2012, MNRAS, 423, 295
Bettoni, D., Galletta, G., Rampazzo, R., et al. 2011, A&A, 534, A24
Bettoni, D., Mazzei, P., Rampazzo, R., et al. 2014, Ap&SS, 354, 83
Blanton, M., & Berlind, A. 2007, ApJ, 664, 791
Boselli, A., Eales, S., Cortese, L., et al. 2010, PASP, 122, 261
Bournaud, F., Jog, C. J., & Combes, F. 2005, A&A, 437, 69
Bremer, M., Phillipps, S., Kelvin, L., et al. 2018, MNRAS, 476, 12
Bressan, A., Panuzzo, P., Buson, L., et al. 2006, ApJL, 639, L55
Buat, V., Takeuchi, T., Iglesia-Páramo, J., et al. 2007, ApJS, 173, 404
Burrows, D. N., Hill, J. E., Nousek, J. A., et al. 2005, SSRv, 120, 165
Buson, L., Bettoni, D., Mazzei, P., et al. 2015, AdAst, 2015, 274968
Calabrese, E., Hlozek, R., Bond, J., et al. 2017, PhRvD, 95, 063525
Caon, N., Capaccioli, M., & D'Onofrio, M. 1993, MNRAS, 265, 1013
Christensen, C., Quinn, T., Governato, F., et al. 2012, MNRAS, 425, 3058
Christensen, C., Quinn, T., Stinson, G., Bellovary, J., & Wadsley, J. 2010, ApJ, 717, 121
Citterio, O., Conconi, P., Ghigo, M., et al. 1994, Proc. SPIE, 2279, 480
Combes, F., Dupraz, C., & Gerin, M. 1990, in Proc. Int Conf. Dynamics and Interactions of Galaxies, ed. R. Wielen (New York: Springer), 205
Courtois, H, & Tully, B. 2015, MNRAS, 447, 1531
Curir, A., & Mazzei, P. 1999, NewA, 4, 1
Curir, A., Mazzei, P., & Murante, G. 2006, A&A, 447, 453
de Vaucouleurs, G. 1948, AnAp, 11, 247
Di Matteo, P., Combes, F., Melchior, A.-L., & Semelin, B. 2007, A&A, 468, 61
Eales, S., Baes, M., Bourne, N., et al. 2018b, MNRAS, 481, 1183
Eales, S., de Vis, P., Smith, M., et al. 2017, MNRAS, 465, 3125
Eales, S., Smith, D., Bourne, N., et al. 2018a, MNRAS, 473, 3507
Eliche-Moral, M., Rodrguez-Prez, C., Borlaff, A., et al. 2018, A&A, 617, A113
Gehrels, N., Chincarini, G., Giommi, P., et al. 2004, ApJ, 611, 1005
Genzel, R., Förster Schreiber, N. M., Rosario, D., et al. 2014, ApJ, 796, 7
Henriques, B., White, S., Lilly, S., et al. 2019, MNRAS, 485, 3446
Hernández-Pérez, F., & Bruzual, G. 2014, MNRAS, 444, 2571
Ho, L. C., Zhao-Yu, L., Barth, A. J., Seigar, M. S., & Peng, C. Y. 2011, ApJS, 197, 21, CGS
Hodges-Kluck, E., & Bregman, J. N. 2014, AJ, 789, 131
Hogg, D., Blanton, M., Brinchmann, J., et al. 2004, ApJL, 601, L29
Jeong, H., Sukyoung, K., Bureau, M., et al. 2009, MNRAS, 398, 2028
Józsa, G. I., Oosterloo, T. A., Morganti, R., Klein, U., & Erben, T. 2009, A&A, 494, 489
Just, D., Zaritsky, D., Sand, D., Desai, V., & Rudnick, G. 2010, ApJ, 711, 192
Kaneda, H., Honaka, T., Sakon, L., et al. 2008, ApJ, 684, 270
Katsianis, A., Blanc, G., Lagos, C. P., et al. 2017, MNRAS, 472, 919
Kauffmann, G., White, S. D. M., Heckman, T. M., et al. 2004, MNRAS, 353, 713
Kaviraj, S., Laigle, C., Kimm, T., et al. 2017, MNRAS, 467, 4739
Kaviraj, S., Schawinski, K., Devriendt, J. E., et al. 2007, ApJS, 173, 619
Kelvin, L. S., Bremer, M. N., Phillipps, S., et al. 2018, MNRAS, 477, 4116
Kim, D. W., Guhathakurta, P., Van Gorkom, J. H., et al. 1988, ApJ, 330, 684
Kroupa, P. 2012, PASA, 29, 395
Kuntschner, H. 2000, MNRAS, 315, 184
Leeuw, L., Sansom, A., Robson, E., Haas, M., & Kuno, N. 2004, ApJ, 621, 837
Li, Z. Y., Ho, L. C., Barth, A. J., & Peng, C. Y. 2011, ApJS, 197, 22, (CGS)
Makarov, D., Prugniel, P., Terekhova, N., Courtois, H., & Vauglin, I. 2014, A&A, 570, A13
Marino, A., Bianchi, L., Rampazzo, R., et al. 2011a, ApJ, 736, 154
Marino, A., Iodice, E., Tantalo, R., et al. 2009, A&A, 508, 1235
Marino, A., Rampazzo, R., Bianchi, L., et al. 2011b, MNRAS, 411, 311
Martin, D. C., Fanson, J., Schiminovich, D., et al. 2005, ApJL, 619, L1
Martin, G., Kaviraj, S., Devriendt, J., Dubois, Y., & Pichon, C. 2018, MNRAS, 480, 2266
Mazzei, P. 2003, MmSAI, 74, 498
Mazzei, P. 2004, arXiv:astro-ph/0401509
Mazzei, P., & Curir, A. 2003, ApJ, 591, 784
Mazzei, P., & De Zotti, G. 1994, ApJ, 426, 97
Mazzei, P., Della Valle, A., & Bettoni, D. 2007, A&A, 462, 21
Mazzei, P., De Zotti, G., & Xu, C. 1994, ApJ, 422, 81
Mazzei, P., Marino, A., & Rampazzo, R. 2014a, ApJ, 782, 53
Mazzei, P., Marino, A., Rampazzo, R., et al. 2014b, AdSpR, 53, 950
Mazzei, P., Marino, A., Rampazzo, R., et al. 2018, A&A, 610, A8
Mazzei, P., Xu, C., & De Zotti, G. 1992, A&A, 256, 45
Mihos, J. C., & Hernquist, L. 1994, ApJL, 437, L47
Mihos, J. C., & Hernquist, L. 1996, ApJ, 464, 641
Naab, T., & Burkert, A. 2003, ApJ, 597, 893
Nanni, A., Bressan, A., Marigo, P., & Girardi, L. 2013, MNRAS, 434, 2390
Panuzzo, P., Rampazzo, R., Bressan, A., et al. 2011, A&A, 528, A10
Plana, H., Rampazzo, R., Mazzei, P., et al. 2017, MNRAS, 472, 3074
Planck Collaboration XVI, 2014, A&A, 571, A16
Querejeta, M., Eliche-Moral, M., Tapia, T., et al. 2015, A&A, 573, A78
Rampazzo, R., Annibali, F., Marino, A., et al. 2011, Ap&SS, 335, 201
Rampazzo, R., Marino, A., Tantalo, R., et al. 2007, MNRAS, 381, 245
Rampazzo, R., Mazzei, P., Marino, A., et al. 2017, A&A, 602, A97, Paper II
Rampazzo, R., Mazzei, P., Marino, A., et al. 2018, Ap&SS, 363, 80
Rampazzo, R., Panuzzo, P., Vega, O., et al. 2013, MNRAS, 432, 374
Rodighiero, G., Daddi, E., Baronchelli, I., et al. 2011, ApJL, 793, L40
Ryan-Weber, E., Webster, R., & Starvely-Smith, L. 2003, MNRAS, 343, 1195
Salim, S., Fang, J. J., Rich, R. M., et al. 2012, ApJ, 755, 105
Salim, S., Rich, R., Charlot, S., et al. 2007, ApJS, 173, 267
Salim, S., & Rich, R. M. 2010, ApJL, 714, L290
Salpeter, E. E. 1955, ApJ, 121, 161
Savoy, J., Welch, G., & Fich, M. 2009, ApJ, 706, 21S
Schawinski, K., Kaviraj, S., Khochfar, S., et al. 2007, ApJS, 173, 512
Schneider, M., Frenk, C., & Cole, S. 2012, JCAP, 5, 30
Serra, P., & Oosterloo, T. A. 2010, MNRAS, 401, L29
Sérsic, J. L. (ed.) 1968, Atlas de Galaxias Australes (Cordoba: Observatorio Astronomico)
Skrutskie, M. F., Cutri, R. M., Stiening, R., et al. 2006, ApJ, 131, 1163

Spavone, M., Iodice, E., Bettoni, D., et al. 2012, MNRAS, 426, 2003
Spavone, M., Iodice, E., Calvi, R., et al. 2009, MNRAS, 393, 317
Spinoglio, L., Malkan, M., & Rush, B. 1995, ApJ, 4543, 616
Stoughton, C., Lupton, R. H., Bernardi, M., et al. 2002, AJ, 123, 485
Taylor, P., & Kobayashi, C. 2015, MNRAS, 448, 1835
Temi, P., Brighenti, F., & Mathews, W. 2009, ApJ, 707, 890
Temi, P., Brighenti, F., Mathews, W., & Bregman, J. D. 2004, ApJS, 151, 237
Thilker, D. A., Bianchi, L., Schiminovic, D., et al. 2010, ApJL, 714, L171
Tinker, J. L., George, M. R., Leauthaud, A., et al. 2012, ApJL, 755, L5
Toomre, A. 1977, in Proc. Yale Univ. Conf., Evolution of Galaxies and Stellar Populations, ed. B. M. Tinsley & R. B. Larson (New Haven, CT: Yale Univ.), 401
Toomre, A., & Toomre, J. 1972, ApJ, 178, 623
Trinchieri, G., Marino, A., Mazzei, P., Rampazzo, R., & Wolter, A 2012, A&A, 545, A140
Trinchieri, G., Rampazzo, R., Mazzei, P., Marino, A., & Wolter, A. 2015, MNRAS, 449, 3021, Paper I
Vega, O., Bressan, A., Panuzzo, P., et al. 2010, ApJ, 721, 1090
Wang, E. X., Taylor, P., Federrath, C., & Kobayashi, C. 2019, MNRAS, 483, 4
Warren, M., Quinn, P., Salmon, J., & Zurek, W. H. 1992, ApJ, 399, 405
Wei, L., Kannappan, S., Vogel, S. N., Baker, A. J., et al. 2010, ApJ, 708, 841
Weigel, A., Schawinski, K., Caplar, N., et al. 2017, ApJ, 845, 145
Wetzel, A. R., Tinker, J. L., & Conroy, C. 2012, MNRAS, 424, 232
Wilman, D. J., Oemler, A., Jr., Mulchaey, J. S., et al. 2009, ApJ, 692, 298
Wyder, T. K., Martin, D. C., Schiminovich, D., et al. 2007, ApJS, 173, 293
Yi, S. K., Lee, J., Sheen, Y. K., et al. 2011, ApJS, 195, 22
Yi, S. K., Yoon, S. J., Kaviraj, S., et al. 2005, ApJL, 619, L111
Young, L., Serra, P., KraJnović, D., & Duc, P.-A. 2018, MNRAS, 477, 2741
Zeilinger, W. W., Pizzella, A., Amico, P., et al. 1996, A&AS, 120, 257